NAVAL POSTGRADUATE SCHOOL

MONTEREY, CALIFORNIA

THESIS

OPTIMIZATION OF LIGHT EXTRACTION FROM HIGH-VOLTAGE SiC PiN DIODE VIA PACKAGE DESIGN

by

John K. Martin II

March 2023

Thesis Advisor: Todd R. Weatherford
Co-Advisor: Matthew A. Porter

THIS PAGE INTENTIONALLY LEFT BLANK

REPORT DOCUMENTATION PAGE	*Form Approved OMB No. 0704-0188*

1. AGENCY USE ONLY *(Leave blank)*	**2. REPORT DATE** March 2023	**3. REPORT TYPE AND DATES COVERED** Master's thesis

4. TITLE AND SUBTITLE OPTIMIZATION OF LIGHT EXTRACTION FROM HIGH-VOLTAGE SiC PiN DIODE VIA PACKAGE DESIGN	**5. FUNDING NUMBERS** REKVV
6. AUTHOR(S) John K. Martin II	

7. PERFORMING ORGANIZATION NAME(S) AND ADDRESS(ES) Naval Postgraduate School Monterey, CA 93943-5000	**8. PERFORMING ORGANIZATION REPORT NUMBER**
9. SPONSORING / MONITORING AGENCY NAME(S) AND ADDRESS(ES) Office of Naval Research, Arlington VA 22203	**10. SPONSORING / MONITORING AGENCY REPORT NUMBER**

11. SUPPLEMENTARY NOTES The views expressed in this thesis are those of the author and do not reflect the official policy or position of the Department of Defense or the U.S. Government.

12a. DISTRIBUTION / AVAILABILITY STATEMENT Approved for public release. Distribution is unlimited.	**12b. DISTRIBUTION CODE** A

13. ABSTRACT (maximum 200 words)

This work demonstrates improving light extraction from a silicon carbide (SiC) PiN diode via package optimization. Previous research has shown that SiC power devices have low on-state voltage drop while maintaining a large breakdown voltage, making them desirable for high-power systems. SiC produces insufficient amounts of electroluminescence due to being an indirect bandgap semiconductor. Device packaging utilizing ray optics can maximize electroluminescent output. A packaging model is developed using computer aided design (CAD) software that supports light production and high-power operation with associated heat and electric potential constraints. The packaged SiC PiN diode is shown to have a light extraction improvement of 1740%. Methods of device production and follow-on testing are also discussed.

14. SUBJECT TERMS SiC, silicon carbide, power converters, donor-acceptor recombination, power device packaging, PiN junction diode, electro-luminescence, wide bandgap, RISF, silicon, Si, CAD	**15. NUMBER OF PAGES** 91
	16. PRICE CODE

17. SECURITY CLASSIFICATION OF REPORT Unclassified	**18. SECURITY CLASSIFICATION OF THIS PAGE** Unclassified	**19. SECURITY CLASSIFICATION OF ABSTRACT** Unclassified	**20. LIMITATION OF ABSTRACT** UU

NSN 7540-01-280-5500

Standard Form 298 (Rev. 2-89)
Prescribed by ANSI Std. 239-18

THIS PAGE INTENTIONALLY LEFT BLANK

Approved for public release. Distribution is unlimited.

OPTIMIZATION OF LIGHT EXTRACTION FROM HIGH-VOLTAGE SiC PiN DIODE VIA PACKAGE DESIGN

John K. Martin II
Lieutenant, United States Navy
BS, United States Naval Academy, 2016

Submitted in partial fulfillment of the
requirements for the degree of

MASTER OF SCIENCE IN ELECTRICAL ENGINEERING

from the

NAVAL POSTGRADUATE SCHOOL
March 2023

Approved by: Todd R. Weatherford
Advisor

Matthew A. Porter
Co-Advisor

Douglas J. Fouts
Chair, Department of Electrical and Computer Engineering

THIS PAGE INTENTIONALLY LEFT BLANK

ABSTRACT

This work demonstrates improving light extraction from a silicon carbide (SiC) PiN diode via package optimization. Previous research has shown that SiC power devices have low on-state voltage drop while maintaining a large breakdown voltage, making them desirable for high-power systems. SiC produces insufficient amounts of electroluminescence due to being an indirect bandgap semiconductor. Device packaging utilizing ray optics can maximize electroluminescent output. A packaging model is developed using computer aided design (CAD) software that supports light production and high-power operation with associated heat and electric potential constraints. The packaged SiC PiN diode is shown to have a light extraction improvement of 1740%. Methods of device production and follow-on testing are also discussed.

THIS PAGE INTENTIONALLY LEFT BLANK

Table of Contents

THIS PAGE INTENTIONALLY LEFT BLANK

List of Figures

THIS PAGE INTENTIONALLY LEFT BLANK

List of Tables

THIS PAGE INTENTIONALLY LEFT BLANK

List of Acronyms and Abbreviations

Al	aluminum
BFOM	Baliga's figure of merit
BV	breakdown voltage
CAD	computer aided design
CV	coefficient of variation
DBC	direct bond copper
E-Ray	extraordinary ray
GaN	gallium nitride
LED	light emitting diode
NPS	Naval Postgraduate School
NRL	Naval Research Laboratory
O-Ray	ordinary ray
PSRC	Power Semiconductor Research Center
RISF	recombination-induced stacking fault
Si	silicon
SiC	silicon carbide
WBG	wide band gap

THIS PAGE INTENTIONALLY LEFT BLANK

Acknowledgments

I would like to say thank you to my advisors, Professor Weatherford and Matthew Porter. Without their guidance, this thesis would never have been finished. I would also like to thank my wife, Marissa, for helping through the good times and the bad and always being a valuable sounding board.

THIS PAGE INTENTIONALLY LEFT BLANK

CHAPTER 1:
Introduction

As U.S. naval technology progresses year after year, there is a growing need to improve power production aboard ships. One way to improve power production is by converting shipboard power distribution from AC to DC main buses, moving away from the larger AC-DC converters currently used to smaller and more efficient DC-DC converters. To implement high efficiency, high power density DC-DC converters, high-frequency switching power electronics are required. In addition, wide band gap (WBG) materials such as silicon carbide (SiC) and gallium nitride (GaN) enable semiconductor devices with low losses, high-temperature operation, and high critical electric field compared with similarly rated Si devices. Therefore, such materials are attractive for next-generation shipboard power electronic systems.

To optimize the control of a DC-DC controller, there must be a way to measure inductor currents and output voltage. One way to accomplish this is by mapping the inherent light production produced by power semiconductor devices during operation to the instantaneous current and temperature of the device. Past work at Naval Postgraduate School (NPS) has shown that bipolar devices fabricated from WBG materials such as GaN and SiC can be used since they produce sufficient amounts of electroluminescence to accomplish this task. However, the electroluminescence made from typically packaged WBG power devices is relatively low due to suboptimal light extraction. The use of WBG power devices for sensing purposes could be viable if packaging could be specifically designed to maximize the extraction of electroluminescence produced by the device alongside typical power device packagings metrics such as heat extraction efficiency and electric field management.

1.1 Research Objectives

This thesis presents the design and fabrication of a novel packaging method for a commercial 10 kV, 50 A SiC PiN diode that maximizes the extraction efficiency of electroluminescence produced by the device. In direct WBG semiconductors, the recombination of holes and electrons conserves energy by releasing a photon. Unfortunately, with indirect semiconduc-

tors, such as silicon (Si) and SiC, the energy is released as a phonon into the lattice structure of the material. This will be discussed in depth in Chapter 2. For the SiC PiN diodes used in this thesis, direct bandgap impurities have been introduced to the diodes, allowing some of the energy to be released as a photon enabling electroluminescent measurements, albeit somewhat poorly. Therefore, a preliminary investigation into the SiC devices is performed to establish a baseline for device characteristics.

Using the preliminary characteristics of the SiC PiN diodes tested in this thesis, device packaging is designed to maximize light extraction while maintaining good thermal conduction and minimizing high electric fringing fields for high-power and high-voltage operation, respectively. This is accomplished by developing an aluminum cradle with an electro-polished interior for a mirror-like finish that is appropriately angled to direct the extracted light. The aluminum cradle is bonded to a direct bond copper (DBC) substrate, and a plano-convex lens is placed above the cradle to direct the light towards a fiber optic cable. The model is developed for design verification in COMSOL computer aided design (CAD) software. Using the built-in physics interfaces, the device is simulated at the maximum power rating. The percentage of light rays converging on the fiber optic cable is estimated along with the thermal conductivity and electric field. Based on these results, the device material is modified to accommodate these constraints for production, and total device improvement is documented.

1.2 Related Work

As power system ratings have continuously increased over the years, higher-rated devices have become highly desired. In the late 1980s, North Carolina State University developed the growth process for SiC, leading to commercial availability of SiC through CREE Research Laboratory [1]. The Power Semiconductor Research Center (PSRC) developed the SiC Schottky barrier rectifiers with early results demonstrating 400 V breakdown voltage (BV) with an on-state voltage drop of 1 V. J. Winkler, J. Homoth, and I. Kallfass investigated electroluminescence production from indirect bandgap materials and current sensing through electroluminescent measurements [2].

Past work at NPS has explored using electroluminescence from power devices to sense device temperature and current for use in power electronic applications. Broeg examined

this using GaN PN power diodes under steady-state conditions [3]. Williams expounded upon Broeg's research to use the electroluminescence of GaN for current estimation and control [4]. Johnston devised a way to use GaN light emission to determine the current and voltage through a buck converter [5]. Robinson examined the light emission from a SiC MOSFET and compared it to a GaN power diode [6].

1.3 Thesis Organization

The basics of semiconductors, WBG materials, diode packaging, and physics of light emission from semiconductors and ray optics are explored in Chapter 2. Chapter 3 presents preliminary device characterization data, packaging design, and device modeling using COMSOL CAD software. Chapter 4 compares the electroluminescence produced before and after device packaging. Finally, Chapter 5 provides an overview of the topics covered by this thesis and discusses future work associated with this research.

THIS PAGE INTENTIONALLY LEFT BLANK

CHAPTER 2:
Background

Semiconductor devices have long been employed in power electronics in everyday life. Semiconductors can be found in computers, communication systems, household appliances, motors, and many more applications providing a means to control power production. Power semiconductor devices have relied primarily upon the use of Si. This is fine for low-power systems in which the losses associated with Si are negligible. For large power systems, such as motors, Si cannot appropriately provide the required power without unacceptable power losses. These losses can be associated with the narrow bandgap of the Si device, which will be covered in further detail in subsequent sections. With Wide Band Gap (WBG) semiconductors, power losses are reduced for equivalent power systems, or similar power losses are achieved with higher power production. The following section further explores how WBG devices improve power systems.

2.1 Wide Bandgap Properties

When comparing different semiconductor materials, it is helpful to compare the different bandgap energies of the devices. For example, Si, which has dominated electronics for over six decades, has a narrow bandgap of 1.12 eV [7]. For narrow bandgap semiconductors to achieve greater voltage ratings, they will have a greater on-state voltage drop [1]. This on-state voltage drop leads to conduction power losses that increase proportionally to the voltage. Therefore, different materials must be used to improve the overall efficiency of a power device that allows for small on-state voltage drops while maintaining high-voltage ratings. One way to accomplish this is by reducing the on-resistance of the semiconductor.

The on-resistance of a semiconductor is a function of the ideal drift region and is given by the equation

$$R_{on} = \frac{W_D}{q\mu_n N_D}, \tag{2.1}$$

where W_D is the width of the ideal drift region shown in Figure 2.1, q is the charge of an electron, and N_D is the doping concentration of the drift region [1].

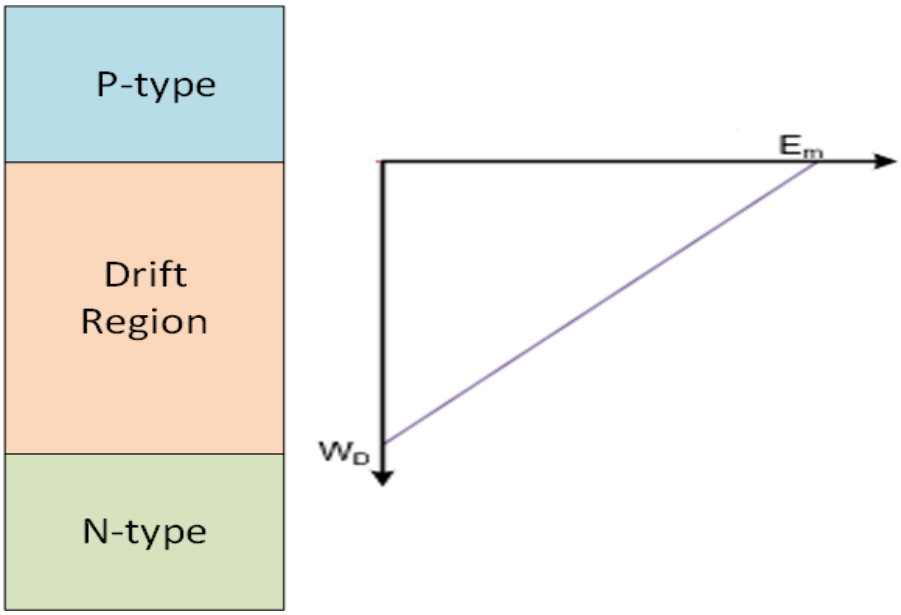

Figure 2.1. The ideal drift region of a PN-junction semiconductor and the relationship between the drift region and the electric field. Adapted from [1]

.

From Figure 2.1, it can be seen there is also a relationship between the drift region and the electric field given by the equation

$$W_D = \frac{2\mathrm{BV}}{E_c}, \tag{2.2}$$

where BV is the breakdown voltage and E_c is the critical electric field [1]. Using (2.2) along with the relationship $N_D = \frac{\epsilon_s E_c^2}{2q\mathrm{BV}}$, (2.1) can be modified to

$$R_{on} = \frac{4\mathrm{BV}^2}{\epsilon_s \mu_n E_c^3}, \tag{2.3}$$

where ϵ_s is the dielectric constant and μ_n is the electron mobility [1]. The denominator of (2.3) is referred to as Baliga's figure of merit (BFOM) ($\epsilon_s \mu_n E_c^3$). The BFOM is often used to determine the material properties of a semiconductor effect upon the resistance of the drift region. When comparing a narrow bandgap semiconductor to a WBG semiconductor,

a narrow bandgap will generally have a worse BFOM, resulting in a higher on-resistance and worse power losses overall. The following section will further show this by comparing Si to SiC.

2.1.1 Physical Properties of SiC

As a WBG material, SiC has a bandgap energy nearly three times that of Si, which corresponds with a critical electric field almost ten times larger and improved thermal conductivity [7]. Electron mobility and the dielectric constant for SiC are 950 $cm^2/V \cdot s$ and 10, respectively, comparable to 1350 $cm^2/V \cdot s$ and 11.9 for Si. A comparison of Si of SiC is shown in Table 2.1 for these and other physical properties.

Table 2.1. Physical properties of SiC versus Si at 27°C. Adapted from [7].

Property	Si	4H-SiC
Bandgap, E_g (eV at 27°C)	1.12	3.2
Critical electric field, $E_c(V/cm)$	$2.5 \cdot 10^5$	$2.2 \cdot 10^6$
Thermal conductivity, (W/cmK at 27°C)	1.5	3–4
Saturated electron drift velocity, vsat (cm/s)	$1 \cdot 10^7$	$2 \cdot 10^7$
Electron Mobility, $\mu_n(cm^2/V \cdot s)$	1350	950
Hole Mobility, $\mu_p(cm^2/V \cdot s)$	480	120
Dielectric constant, ϵ_s	11.9	10
BFOM (normalized to Si)	1	403.2

It should be immediately evident from Table 2.1 that since the BFOM from SiC is over 400 times better than Si there will be a vast improvement in the on-resistance. For example, using an equivalent value for BV in (2.3) and assuming an on-resistance of 1 Ω for a Si device, the on-resistance for a comparable SiC device would be 2.48 mΩ. Therefore, using SiC instead of Si will produce lower power losses and improve overall system performance.

2.1.2 Electroluminescence of SiC

When an external stimulus is supplied to a semiconductor, there is a disturbance of equilibrium through the generation and recombination of electron and hole pairs. Once this stimulus is removed, the device returns to the equilibrium concentration with a recovery time dictated by the recombination of excess carriers [1]. The band structure of the device determines the method via which the recombination of excess carriers occurs. There are two types of electronic structure in semiconductor materials: indirect and direct bandgap. Direct bandgap semiconductors such as GaN have the lowest energy point of the conduction band where the effective momentum is equal to zero. Semiconductors that do not have this property are called indirect bandgap semiconductors, such as Si. A comparison is shown in Figure 2.2.

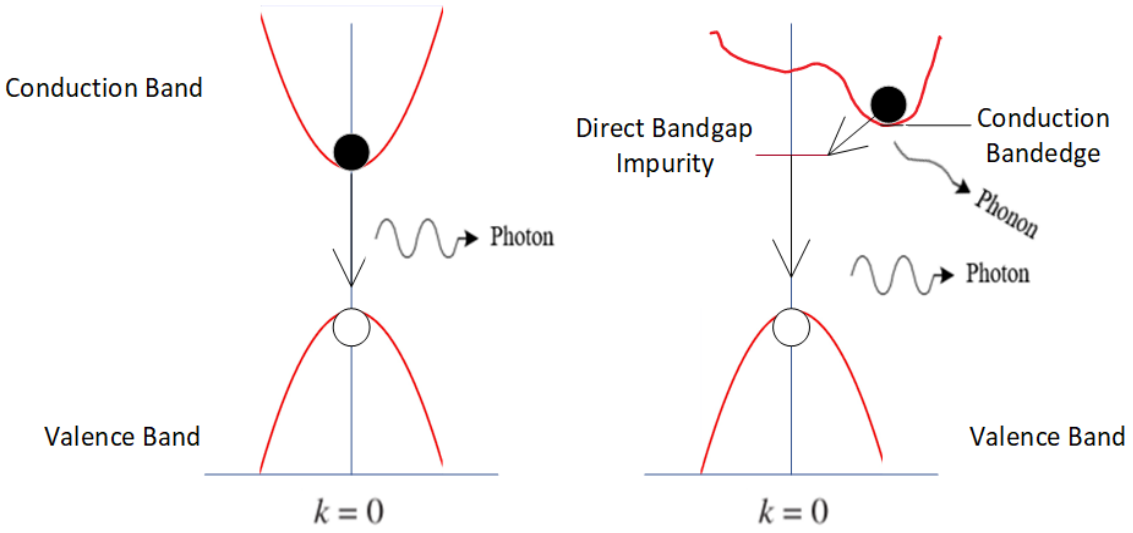

Figure 2.2. Direct bandgap semiconductors have the lowest energy point for the conduction band at k=0 where $\hbar k$ is the effective momentum. Indirect bandgap semiconductors have the lowest energy point for the conduction band where $k \neq 0$. Adapted from [8].

During the recovery time for the device to return to equilibrium, electrons from the con-

duction band recombine with holes from the valence band. To conserve energy during recombination, a photon is emitted from the recombination in a process called radiative recombination if the semiconductor has a direct bandgap structure. If the band structure is indirect, energy is released as a phonon into the lattice of the material in a process called multi-phonon recombination. The energy may also be transmitted into a new electron or hole in Auger recombination. When an indirect material such as SiC has direct bandgap impurities introduced to it, all three processes are present in the material. A photon is released as a direct bandgap material, and a phonon is released into the lattice of the material. This makes material such as SiC a poorer electroluminescent device than a direct bandgap semiconductor but better than material such as Si.

2.1.3 SiC PiN Diode Characteristics

As discussed at the beginning of the chapter, electronic circuits require power devices to control voltage output and current direction. Si Schottky rectifiers, for example, are useful unipolar devices for power systems due to the low on-state voltage drop and fast switching behavior. However, the on-state voltage drop increases substantially as the BV increases over 200 V [1]. As power systems such as motor systems require voltages higher than 200 V, PiN rectifiers can be a preferred choice. SiC PiN diodes can be operated at voltages ranging from 3 to 5 kV with equivalent on-state voltage drops as the Si Schottky rectifier counterpart.

For PiN diodes, the drift region of a PN-junction has a low N-type doping concentration referred to as an i-type region [1]. Unlike Schottky diodes with a metal-semiconductor junction, PiN diodes have the semiconductor-semiconductor junction required for radiative recombination [9] discussed in the previous subsection. For high voltage operations, PiN diodes utilize high-level injection of minority carriers as the current transport. This type of current transport injects a higher concentration of minority carriers than the background drift region doping concentration. With charge neutrality, the number of electrons and holes must become equal. Therefore, the leftover free carriers reduce the resistance of the drift region, allowing a high-current density through the drift region while maintaining a low on-state voltage drop.

2.2 Ray Optics

To design a package to optimize the light extraction from the semiconductor device, first light propagation must be understood. Light propagation follows Fermat's Principle, which describes how light travels the path that takes the least amount of time [10]. Ray optical physics uses Fermat's Principle to establish the governing equations of light motion presented in this section.

2.2.1 Refraction and Reflection

As light travels through a medium, the speed with which it travels changes inversely proportional to the index of refraction, shown as (2.4),

$$n = \frac{c}{v}, \tag{2.4}$$

where n is the index of refraction, c is the speed of light in a vacuum, and v is the speed that light travels in the medium [10]. Air has an index of refraction of 1.0003, which is usually approximated to 1, the refractive index of a vacuum. As light travels from one medium to another, the light is refracted by an angle referred to as the angle of refraction shown by

$$n_1 \sin\theta_1 = n_2 \sin\theta_2, \tag{2.5}$$

which is referred to as Snell's Law of Refraction [10]. θ_1 represents the angle of incident on the material and θ_2 is the angle of refraction shown in Figure 2.3.

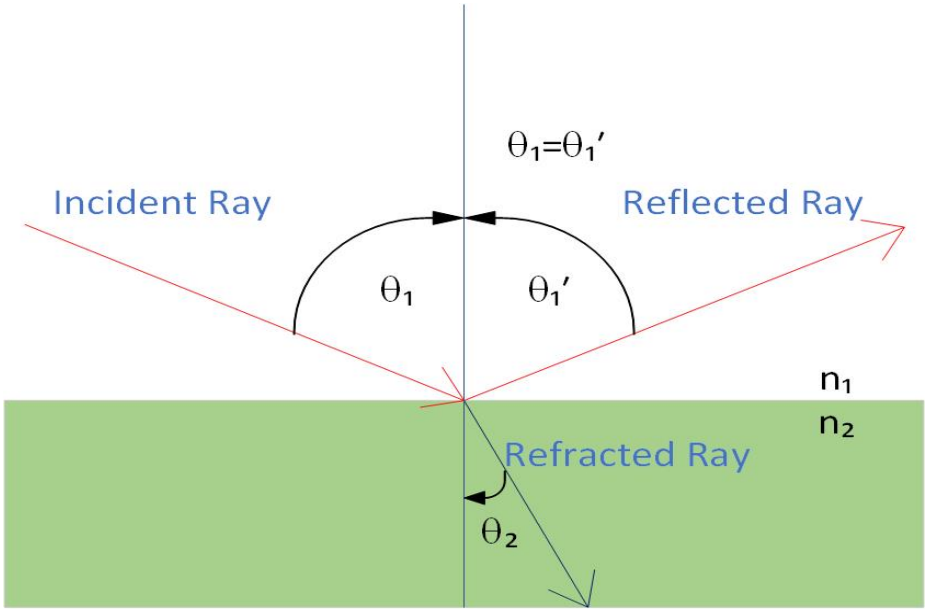

Figure 2.3. A ray passing from one medium to a different medium. Adapted from [10].

If the medium is transparent, the refractive index becomes a function of wavelength and is represented as Sellmeier formula [11].

$$n(\lambda) = \sqrt{1 + \sum_j \frac{A_j \lambda^2}{\lambda^2 - B_j}} \tag{2.6}$$

Equation 2.6 has been fitted as a function of wavelength for many materials and compiled in several databases [12]. One aspect that changes the equation for a given material is which type of ray is solved. When light strikes a surface of the material, it can split into separate beams referred to as ordinary rays and extraordinary rays [10]. The two rays travel at different speeds since they have mutually perpendicular polarization and travel in different directions resulting in small changes in the refractive index of a material. This falls back to (2.4) since the refractive index is a function of the speed of light in the material.

Some light rays will be reflected and not transmitted due to the angle of incident and the

refractive index of the medium. This is a byproduct of Snell's Law of Refraction represented by (2.7) and is referred to as the critical angle [10].

$$\theta_c = \arcsin \frac{n_2}{n_1} \tag{2.7}$$

The light is not transmitted and only reflected if the incident angle is greater than the critical angle, as seen in Figure 2.4. For example, if a light emitting device, such as a light emitting diode (LED), has a small critical angle, then only a small percentage of light will transmit, causing it to appear dim.

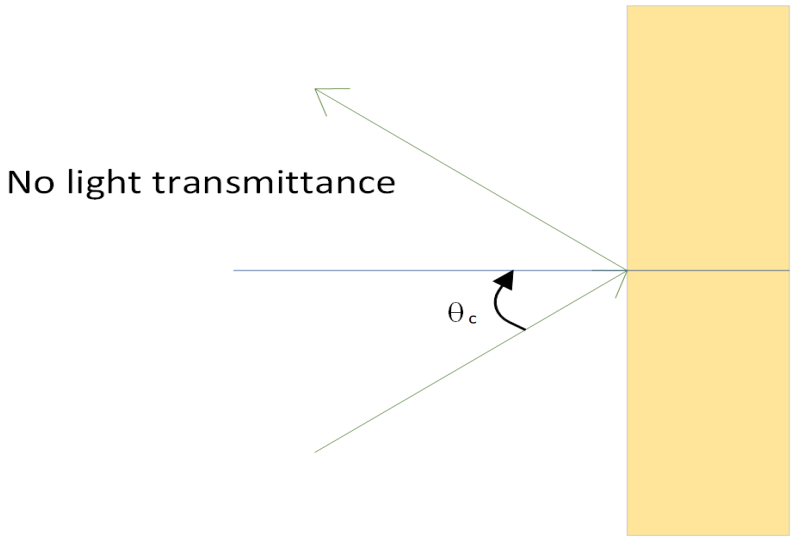

Figure 2.4. When the incident angle equals or is greater than the critical angle, the incident ray is completely reflected. Adapted from [13].

Another property demonstrated in Figure 2.3 is that the angle of incident equals the angle of reflection. This is referred to as the Law of Reflection shown by (2.8) [10].

$$\theta_1' = \theta_1 \tag{2.8}$$

From (2.8), the angle of incident equals the angle of reflection. This property is beneficial when using light against mirrors or mirror-like surfaces. By angling and combining mirrors,

the light a source produces can be directed in most directions as required.

2.2.2 Fresnel Equations

From the equations in Section 2.2.1, the angle of reflection and refraction can be determined, but the equations do not show how much light is transmitted. To calculate the amount of transmittance, the Fresnel Equation for transmittance is utilized

$$T = \frac{n_2 \cos\theta_2}{n_1 \cos\theta_1} t^2 \text{x}100\%, \tag{2.9}$$

where T is the percent of light transmitted and t is the transmission coefficient [13]. The transmission coefficient is inversely proportional to the incident angle and is at a maximum when $\theta_1 = \theta_2 = 0°$. This gives the modified equation

$$T = \frac{4n_1 n_2}{(n_1 + n_2)^2} \text{x}100\%, \tag{2.10}$$

which has a maximum value of 100% when the two materials have the same refractive index. If one refractive index is much greater than the other, $n_1 >> n_2$, then transmittance becomes approximately equal to $\frac{4}{n_1}$.

2.2.3 Optical Lens

With the Law of Refraction, as light passes from the air through the lens and back to the air, the light rays bend. Lenses utilize this property to direct the light rays. Depending on design constraints, the lens shape can be designed to have a set focal point for light convergence. To calculate the focal point, the Lens-Maker's Equation is used [10].

$$\frac{1}{f} = \left(\frac{n}{n_{air}} - 1\right)\left(\frac{1}{r_1} - \frac{1}{r_2}\right) \tag{2.11}$$

In (2.11), f is the focal length, r_1 is the radius of one side of the lens closest to the focal point, and r_2 is the radius of the other side of the lens, as shown in Figure 2.5.

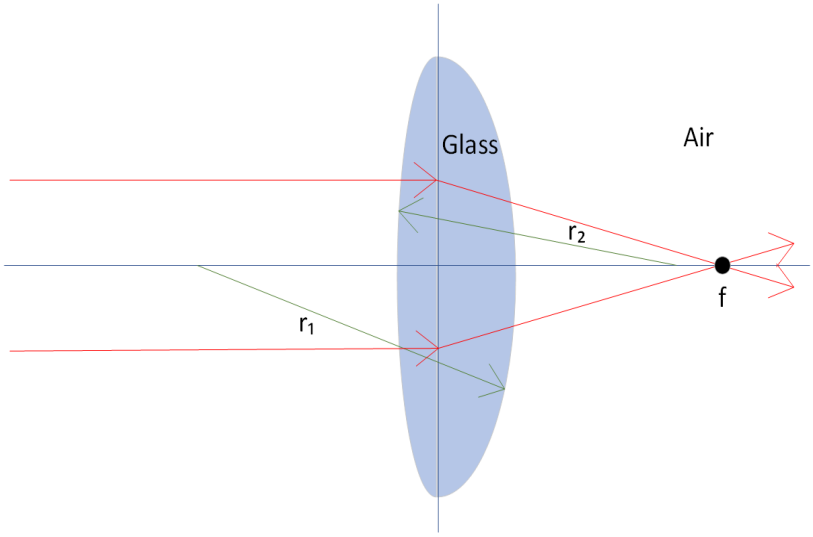

Figure 2.5. Light rays interacting with a convex lens of different radii. Adapted from [10].

If the light rays interacting with the lens are parallel, the lens can be shaped as a plano-convex lens to make the rays converge at the same point [14]. This is done by the lens asymmetry where one side is near flat, and the other has a large radius. The plano-convex shape is handy when maximizing light gathering and limiting attenuation. This type of lens will be exploited in Chapter 3 when converting from a traditional power device packaging design to one optimized for light production.

2.3 Power Device Packaging Design

The usual priorities for traditional power device packaging design are to maximize power output and heat extraction, sustain high electric field strengths, and minimize losses. However, as Si power devices have reached the theoretical performance capabilities, WBG materials such as SiC have been extensively researched for use in power devices due to the advanced capabilities outlined in Section 2.1 and are packaged as shown in Figure 2.6.

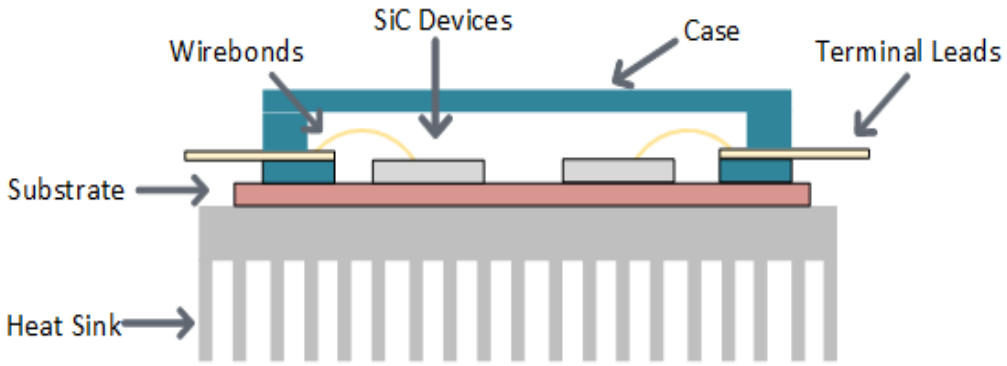

Figure 2.6. Traditional power device packaging consists of a power device attached to a DBC substrate and wire bonded to terminals. The device usually has some way to extract heat and is represented with a fin-type heat sink in this generic representation. Adapted from [15].

Unfortunately, with greater capabilities associated with WBG materials, such as high switching speeds, considerations have to be given regarding parasitic inductances [15]. These parasitic inductances result in more significant voltage transients and ringing, leading to greater device losses. The parasitic inductances in commercial use typically range between 15–30 nH. Methods proposed to improve the parasitic inductances include using wireless and different layered structures and changing the die-attaching materials and bonding types.

As mentioned at the beginning of this section, it is often desired for a power device to sustain high electric field strengths for high-power operation. There is a limit, though, to how high an electric field can be. Surrounding a typical device is air, with a dielectric strength of 3 MV/m [10]. A dielectric breakdown can occur if the electric field strength outside the substrate exceeds that of air. With dielectric breakdown, the air molecules become ionized and turn into conductors. When the molecules conduct, there is a discharge of electricity known as an arc discharge. An arc discharge can lead to damage to equipment or device failure. Therefore, considerations need to be made to prevent dielectric breakdown when developing a power device that needs to operate in a high-power environment.

Another issue with the generic device design shown in Figure 2.6 is the lack of optimization

for electroluminescent extraction. This is primarily due to light extraction not being a priority in most power devices. However, this inherent light production can be exploited for current and temperature measurements. This thesis, therefore, seeks to improve upon the generic design shown in Figure 2.6 by adding a mirrored cavity for a SiC PiN diode, encapsulating the die with optically-optimized epoxy, and adding a lens for light direction. In addition, various device structures and materials will be explored to minimize power losses and parasitic inductances and maximize heat extraction while maintaining a high electric field for high-power operations.

This will be accomplished in Chapter 3 along with exploring the electroluminescent constraints of a SiC PiN diode developed by CREE Research Laboratory. Following the device limitation exploration, methods to improve the light extraction will be discussed using the ray physics shown in Section 2.2. Chapter 3 describes the production of a simulated device packaging that will improve light extraction efficiency.

CHAPTER 3:
Preliminary Testing, Experimental Design, and Modeling

3.1 Bare SiC Diode Testing

One out of 12 unpackaged SiC PiN diodes developed by CREE Research Laboratory was used for the tests conducted in this chapter. Each chip is 8.7 mm x 8.7 mm x 0.5mm and is rated at 50 A and 10 kV [16]. The forward conduction of the diodes is represented in Figure 3.1.

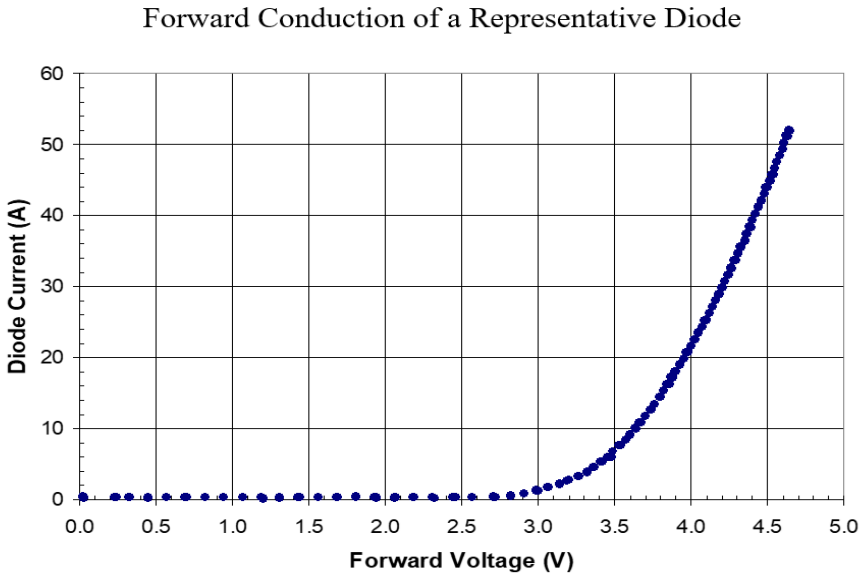

Figure 3.1. Forward voltage versus diode current for SiC PiN diodes. Source: [16]. The on-state voltage drop is approximately 3.58 V. Using the slope of the IV line, the on-resistance is 0.0219Ω.

The diode was placed in a Signatone S-1160 Probe Station on top of a temperature-controlled

gold-plated chuck to get a preliminary idea of the effects of current and temperature.

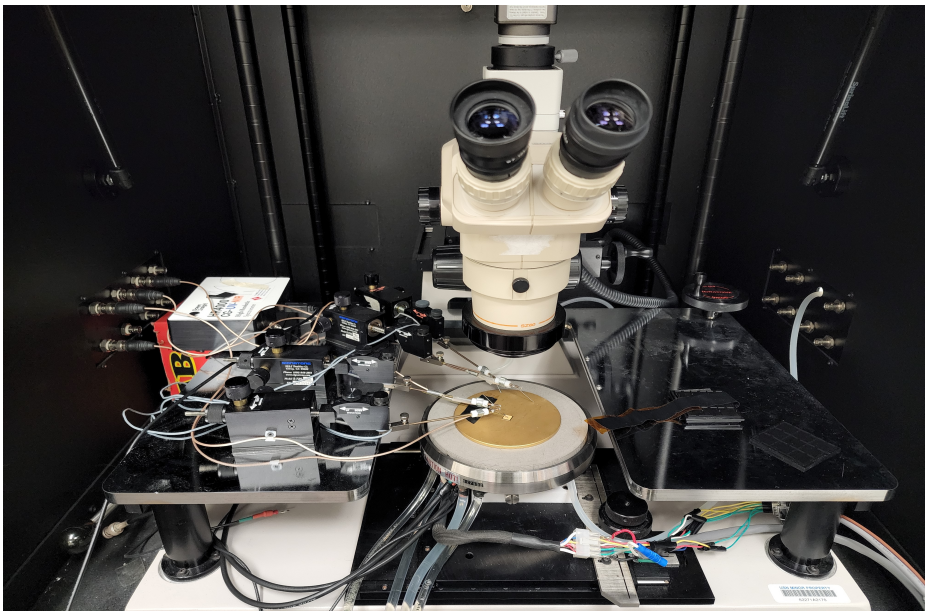

Figure 3.2. The setup of the Signatone S-1160 Probe Station for the lab experiments in Chapter 3.

The diode was connected to two PSS-2005 Programmable Power Supplies in parallel to achieve currents over 5 A. An H1000 Thermal Chuck System and a C1000 Heat Exchanger were connected to the probe station to hold the diode at varying temperatures. This was used to determine the connection between temperature, light emission intensity, and wavelength. A fiber optic cable was fabricated to sit flush with the diode and connected to an Ocean Insight HR4000 spectrometer to measure the electroluminescence intensity spectrum.

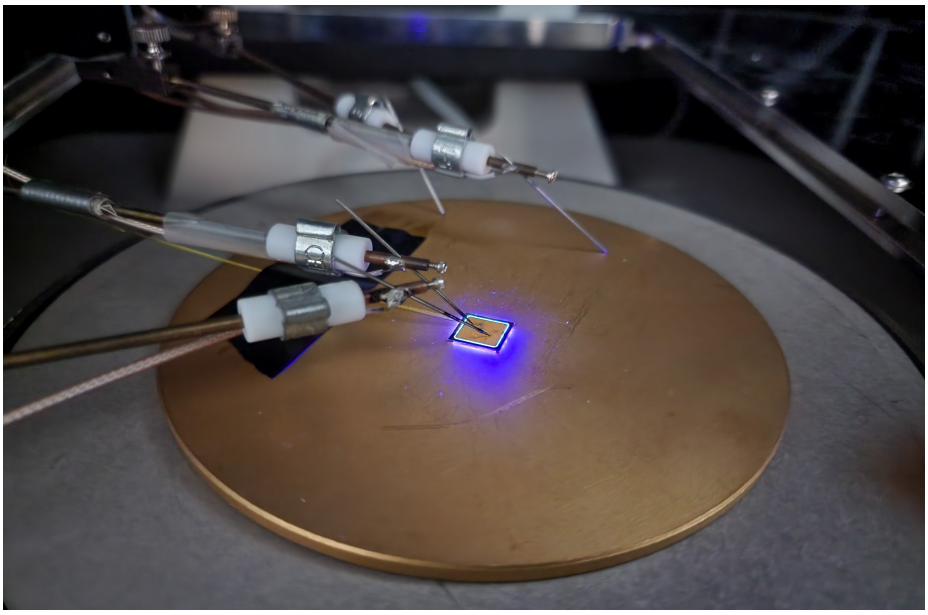

Figure 3.3. SiC PiN diode with approximately 3 A of supplied current.

With one of the diodes properly connected, multiple test runs were carried out over several days. Each test run consisted of measurements at four temperatures with different current settings. The runs were averaged to help reduce daily variance from weather, humidity, temperature, and other miscellaneous effects.

3.1.1 25°C Electroluminescence Measurements

For the first round of tests conducted, the thermal chuck was set to 25°C. This is slightly higher than ambient temperature, but due to a lack of temperature stability in the laboratory, there was no reliable method for a baseline test without using the temperature controls. Once the required controls were in place, the SiC PiN diode was biased with 1 A of current through the anode. After the temperature stabilized, the electroluminescent spectrum was measured. The current was then increased to 3 A, 5 A, 7.5 A, and finally 10 A, with measurements conducted at each phase once the temperature of the device stabilized. The measured electroluminescence spectra as a function of current are shown in Figure 3.4.

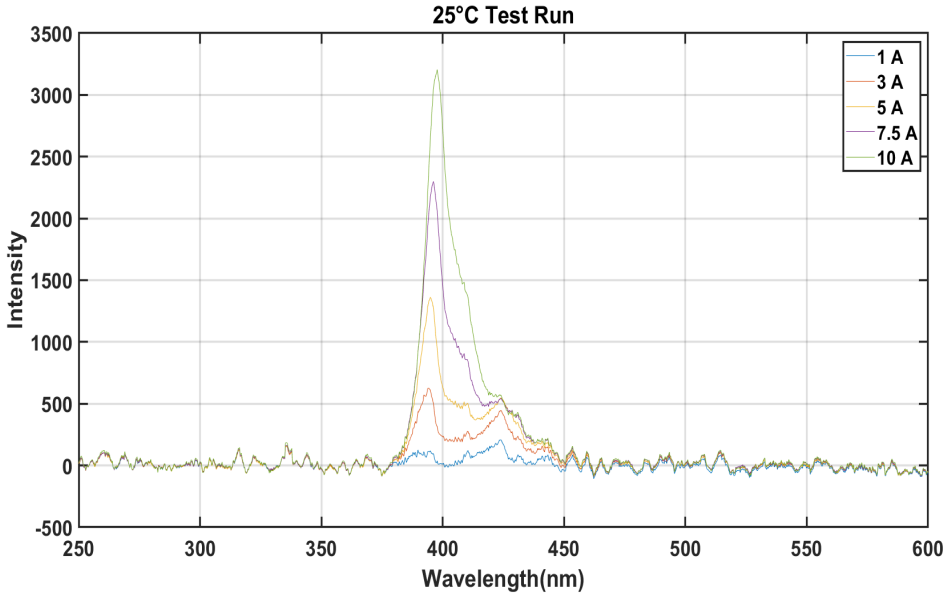

Figure 3.4. 25°C test run at 1 A, 3 A, 5 A, 7.5 A, and 10 A.

From Figure 3.4, the primary peak is around 395 nm with a secondary peak at approximately 424 nm. As the current increases, the 395 nm peak experiences redshifting which will become more pronounced at higher temperatures. Due to the low-level production of light in SiC materials, as discussed in Section 2.1, the 395 nm peak cannot be fully distinguished from background noise until 3 A of current. The 424 nm peak is due to intrinsic stacking faults that occur in SiC [17]. These defects are referred to as recombination-induced stacking fault (RISF). Unlike the 395 nm peak, the RISF peak does not redshift as temperature increases, nor does it continuously increase in intensity, as shown by the peak reaching a maximum intensity with 5 A of current.

3.1.2 75°C Electroluminescence Measurements

For the second round of tests, the temperature of the thermal chuck was set to 75°C, and current values of 3 A, 5 A, and 10 A were supplied to the diode. The measured electroluminescence spectra are shown in Figure 3.5.

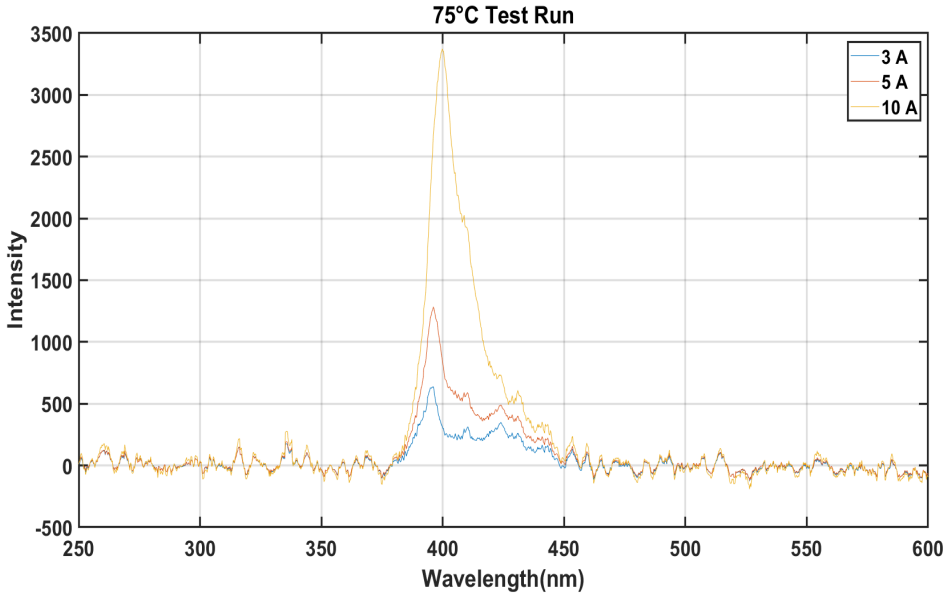

Figure 3.5. 75°C test run at 3 A, 5 A, and 10 A.

As mentioned in Section 3.1.1, the higher temperature leads to a redshift of the primary peak that further shifts in position with the magnitude of the applied current, particularly at 10 A. It should be noted that the peak caused by RISF is far less pronounced than it was at 25°C. A positive byproduct of this reduction is that the primary peak is now more discrete, especially at the lower currents where the RISF peak was a more significant issue.

3.1.3 100°C Electroluminescence Measurements

For the third round of tests, the temperature of the thermal chuck was increased to 100°C, and the same currents as the second round of tests were applied to the diode. The measured electroluminescence spectra are shown in Figure 3.6.

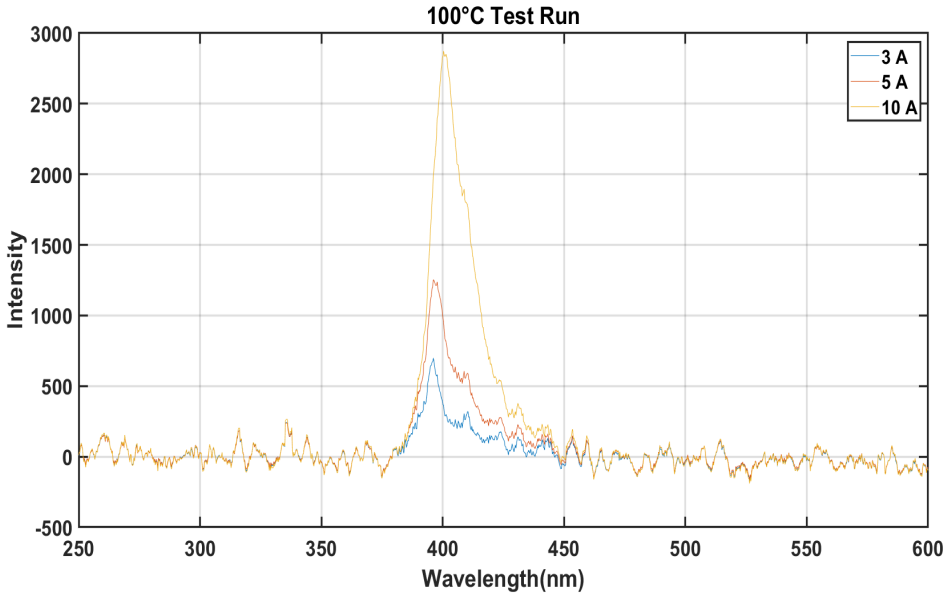

Figure 3.6. 100°C test run at 3 A, 5 A, and 10 A.

Once again, the primary peak redshifts in proportion to the applied current while the RISF peak decreases proportionally with the increased temperature. Unlike the previous test run, there is a noticeable drop in the intensity of the primary peak, especially at 10 A. The 3 A and 5 A peaks are about 2% lower, and the 10 A peak is 17% lower than the previous test run. This decrease will be further examined in the final test run.

3.1.4 125°C Electroluminescence Measurements

For the final round of testing, the temperature of the thermal chuck was increased to 125°C, and the same currents as the previous two test runs were applied. The results of these measurements are shown in Figure 3.7.

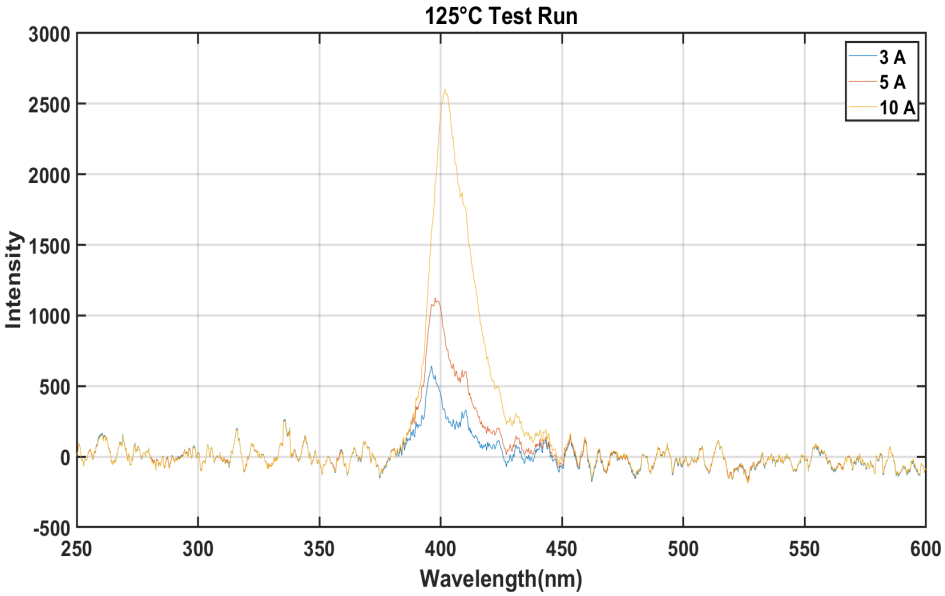

Figure 3.7. 125°C test run at 3 A, 5 A, and 10 A.

As expected, the primary peaks are further redshifted, and the RISF peaks are further decreased. The intensity of the primary peaks decreased, once again, proportionally with the increased temperature, with the most significant decrease occurring with the highest current. This is seen with the 10 A peak falling by another 9% while the 3 A and 5 A peaks reduced by about 1 to 2%. All the above test runs will be further analyzed in Chapter 4 to develop device packaging that will increase the light output at all current levels, reduce the heat output, and lower any background noise detected. A linear equation from the bare model will also be approximated that relates the current and temperature to the light intensity. This equation will act as a baseline to compare to a post-produced device packaging for future work.

3.2 Determining a Baseline in Light Production

Using the data collected from Section 3.1, it was determined that the 395 nm peak was the ideal peak to focus on. Due to the limited light intensity from the bare device, an encapsulation had to be designed that would improve the light produced, direct the light to a

spectrometer through a fiber optic cable, and had to be able to handle high levels of current and voltage.

3.2.1 Computing the Refraction Index of SiC

As the refraction index of a material is dependent on the wavelength, the first step was to compute a theoretical value for the refraction index from 395 nm to 405 nm to account for redshifting. To approximate the refractive index, Sellmeier Equation 2.6 can be used. Two equations can be compared, with one being for an extraordinary ray (E-Ray) (3.1) [18] and the other for an ordinary ray (O-Ray) (3.2) [19], respectively.

$$n_e = \sqrt{6.79485 + \frac{0.15558}{\lambda^2 - 0.03535} - 0.02296\lambda^2} \tag{3.1}$$

$$n_o = \sqrt{1 + \frac{0.20075\lambda^2}{\lambda^2 + 12.07224} + \frac{5.54861\lambda^2}{\lambda^2 - 0.02641} + \frac{35.65066\lambda^2}{\lambda^2 - 1268.24708}} \tag{3.2}$$

Silvaco Inc. has experimental values for SiC that were used to compare with the theoretical values computed using (3.1) and (3.2). A plot was formed to show how they vary in Figure 3.8.

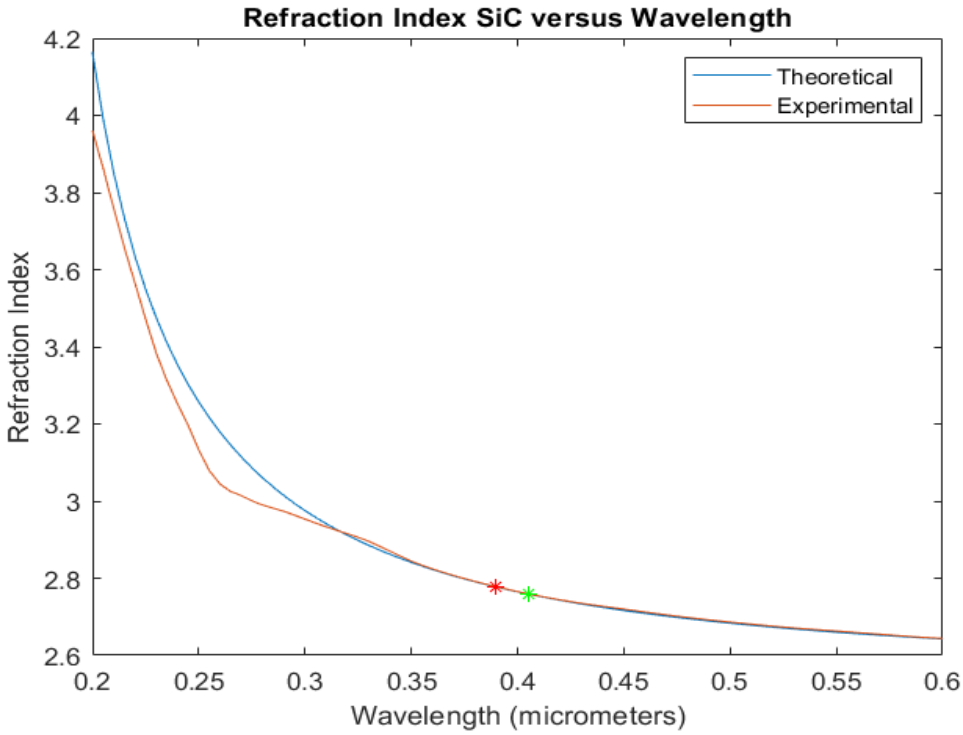

Figure 3.8. The Refraction Index of SiC as function of wavelength. A red star highlights 395 nm, and a green star highlights 405 nm.

Figure 3.8 shows a significant deviation below 300 nm for the theoretical and experimental values. However, there is little distinction between the two graphs at the interval between 395 nm to 405 nm. Considering this range, the refractive index can vary from 2.76 to 2.77.

3.2.2 Losses Associated with Light Production From the Unpackaged Device

Now that there is an interval for the refractive index of SiC, the number of light rays detected by the spectrometer could be determined. First, the amount of light released from the device had to be determined using (3.3),

$$\eta_{extraction} = \frac{1}{4}\frac{{n_2}^2}{{n_1}^2}, \tag{3.3}$$

where n_1 is the refractive index of the first medium, and n_2 is the medium the ray of light passes into [9]. Equation 3.3 is an approximation used to determine LED efficiency. Using $n_1 = 2.77$ and $n_2 = 1$, the amount of light produced that was released by the SiC diode was determined to be about 3.25%. Using (2.7), θ_c was determined to equal 22.2°. Next, the transmittance had to be determined using (2.9). Using an angle of incident equal to zero and the modified (2.10), with the same n_1 and n_2, the transmittance was computed to be 75%. By noting that the diameter of the fiber optic cable is 440μm, the cable could only pick up 1.26% of the light released in a perfect setting. Therefore, the total amount of light detected at best is only 0.31%.

3.3 Designing the Device

To improve the constraints in Section 3.2.2, an encapsulation material would need to be used to help taper the refractive indices between the device and air, and more light would need to be directed towards the fiber optic cable.

3.3.1 Tapering the Refractive Index

To taper the refractive indices between the SiC and the fiber optic cable, a material has to be inserted between the diode and the fiber optic cable. The best case scenario would be to layer materials that would taper down linearly from the refractive index of SiC to that of air in a short distance, as seen in Figure 3.9.

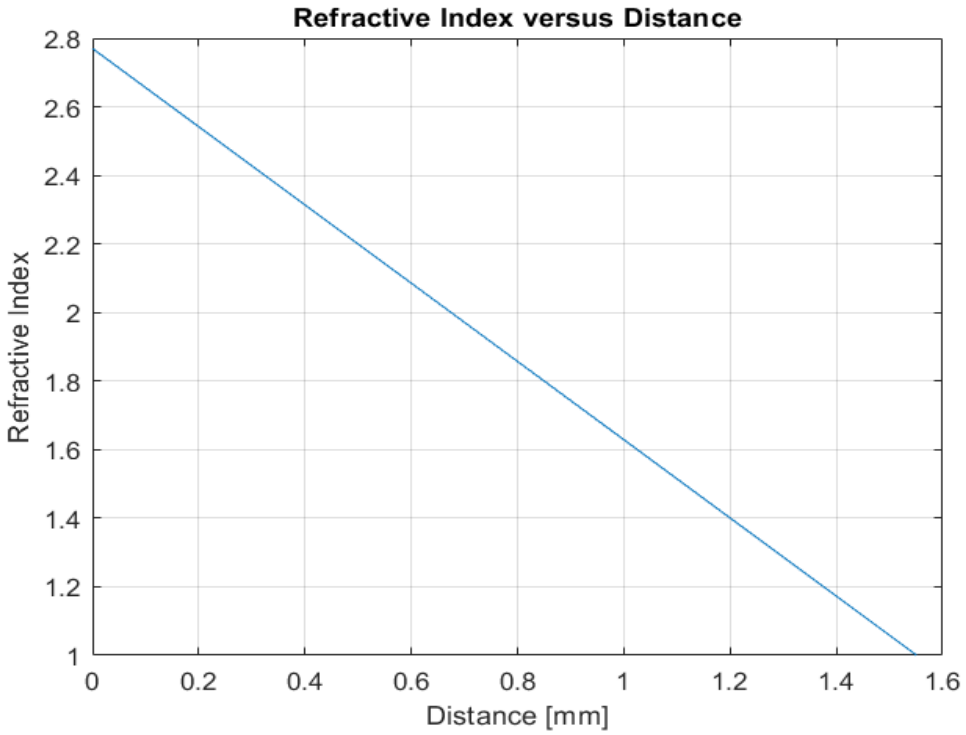

Figure 3.9. Linear tapering of the refractive index from that of SiC to air.

Were this feasible, the transmission losses would be negligible. Unfortunately, this is not possible. The closest set-up for linear tapering would be by taking glasses of incrementally decreasing refractive indices with minuscule widths and then layering the glass around the device. While possible, the glass approach would be expensive since each glass would have to be custom-made, and the fabrication of the device would be much more complex due to the layering of the glass, rendering this approach impractical. In light of this, the best approach would be to find a material for encapsulation with a refractive index in-between that of the SiC and air. Using Figure 3.9 as a reference, the optimal refractive index would be $n_{material} = 1.89$. However, since finding an exact refractive index equal to 1.89 is unlikely, a range was used as a search parameter $n_{material} = 1.4 : 2.0$.

3.3.2 Encapsulation Material

Besides the refractive index consideration, the encapsulation material has to allow light to pass through and not become opaque at higher temperatures. As most epoxy resins are either opaque or become discolored at higher temperatures, choices were limited. The best option is 20-3401 Medical, Optical, and Semiconductor Grade Epoxy Resin. With 20-3401, the epoxy allows greater than 94% transmission from 300 nm to 400 nm and 99% transmission greater than 400 nm [20]. Its operating temperature range is from -45°C to 150°C with an intermittent allowance of up to 300°C. It also has a refractive index of 1.532. This is on the lower end of the search range, but the limitations were considered tolerable as it is designed for optical use. Using the new refractive index in (2.9), the transmittance increased from 75.1% to 87.7%. While a layered approach would have gotten the transmittance in the high 90% range, using 20-3401 will be the more economical approach.

3.3.3 Choosing the Material and Shape of the Diode Cavity

When designing the cavity, the diode would be encapsulated within; there were several constraints to keep in mind:

1. Since the SiC PiN diode is already large, the cavity size had to be minimized to ease fabrication.
2. The walls had to be angled such that the light could be directed to a fiber optic cable.
3. The device needed to allow a lens to be placed on top to focus the light.
4. The device needed to conduct heat well enough to keep the epoxy from overheating.

With the above considerations, the initial design choice was to use an etched Si wafer with walls of the well angled at 45°. The choice for the wall angles came from using the Law of Reflection, (2.8). As light would be traveling perpendicular to the sides of the SiC diode, the light needed to interact with the walls of the cavity at 45° to reflect at 45°. This would produce light rays that are 90° from the initial projection, as shown in Figure 3.10.

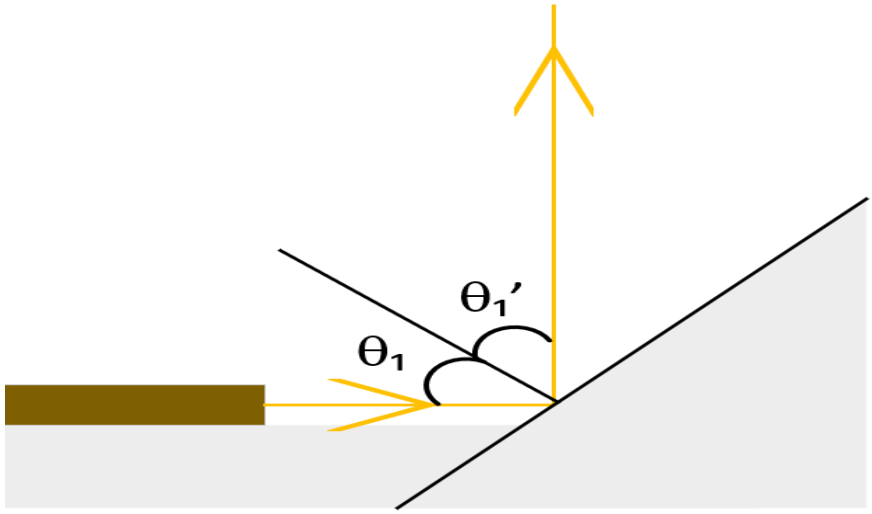

Figure 3.10. With light produced in line from the light emitting source has an incident angle of 45° on a reflective surface, it produces a light perpendicularly to the original direction.

To determine the size of the Si wafer, the top of the cavity was treated as the base of a pyramid, and the diode pad was treated at an intersection plane on the pyramid shown in Figure 3.11.

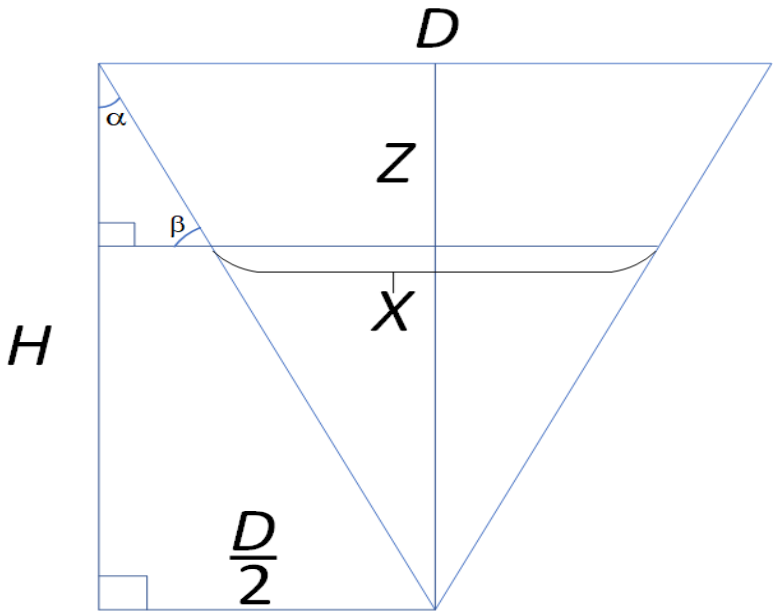

Figure 3.11. H is the height of the entire pyramid, z is the height of the cavity for the diode, and D is the length of the top of the cavity.

Since the cavity width and the diode pad size is known — 12 mm and 10.44 mm — an appropriate depth could be calculated that would give 45° walls. First, the height had to be solved by using (3.4).

$$H = \frac{D}{2\tan\alpha} \tag{3.4}$$

Using D = 12 mm and α = 45°, H becomes 6 mm. With H known, the cavity depth could be found using (3.5).

$$z = H - \frac{x\tan\beta}{2} \tag{3.5}$$

With H = 6 mm, x = 10.44 mm, and β = 45° the cavity depth becomes 0.78 mm. Since the wafer has to be larger than the cavity depth, a wafer thickness of 1.5 mm was deemed appropriate. The final design choice is a rectangle with a length of 17 mm and a height of 1.5 mm.

After much consideration, it was determined that using a Si wafer would not work. This is because the etching chemicals required to etch the cavity anisotropically would take several minutes due to the depth of the cavity, causing degradation of the design mask before completion, rendering the desired shape impossible. A fabricated metal cavity was determined to be the best solution to this problem as no etching would be required [21]. The most viable candidate for the metal would be aluminum due to its economic benefits and thermal properties. After fabrication, the metal cavity would be electro-polished and then coated with silver on the inside of the cavity. This would give the cavity a mirror-like finish required to direct the light shown in Figure 3.10.

3.3.4 Choice of Lens

To direct the vertical light to a single point, a plano-convex lens would have to be chosen with a relatively short focal length to limit attenuation. Given that constraint, a 12.7 mm diameter BK-7 lens with a focal length of 15 mm was the best option [22]. The refractive index was determined similar to that of SiC by using (3.6) [23].

$$n = \sqrt{1 + \frac{1.03961212\lambda^2}{\lambda^2 - 0.00600069867} + \frac{0.231792344\lambda^2}{\lambda^2 - 0.0200179144} + \frac{1.01046945\lambda^2}{\lambda^2 - 103.560653}} \tag{3.6}$$

Given the distance between the lens and the fiber optic cable, the light attenuation will be worse than in the unpackaged case, as the fiber optic cable could be placed flush with the device. However, with the improvement in directing light rays into the fiber optic cable, the effect of attenuation should be reduced.

3.3.5 Final Device Design

With the calculated information from the previous sections, a theoretical model of the device can now be devised. Taking the encapsulated diode, the aluminum well would be sodered to a DBC substrate, such as AI203 or AIN. Two smaller copper pads would also be soldered to the board as a positive and negative port for the diode. Gold wires would then be attached from the copper pads to the diode, with one set directly in contact with the top of the diode as a positive side and the other set connected to the outside of the metal cavity. Finally, a plastic lens holder would hold the lens above the device. This is modeled in Figure 3.12.

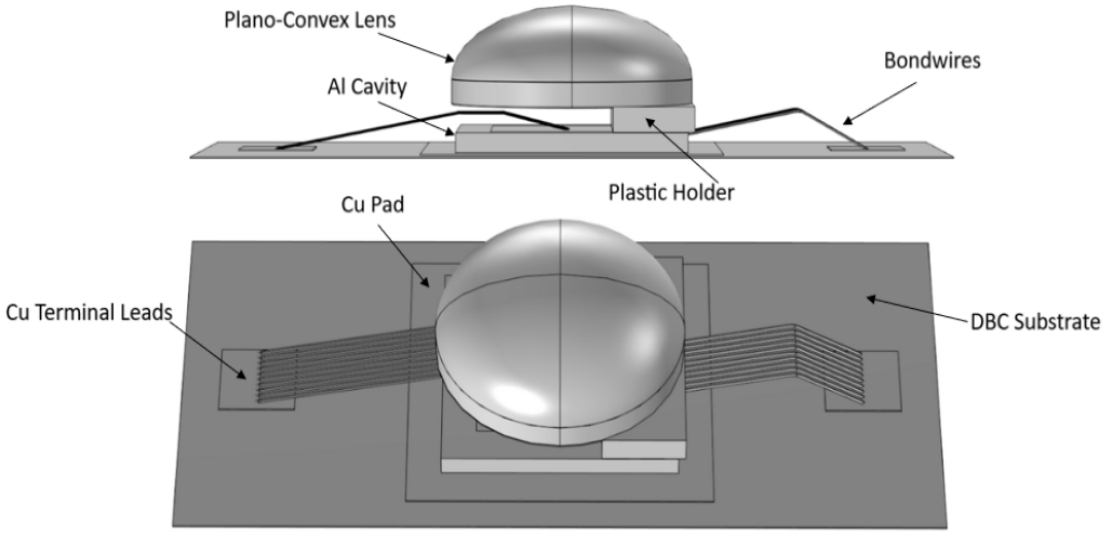

Figure 3.12. The top image is a side profile of the proposed device modeled using COMSOL. The bottom image is a slanted view to show the top of the device.

With the device shown in Figure 3.12, the theoretical amount of light expected to be detected is 5.85%. Compared to the 0.31% received from the unpackaged diode, the improved design will allow 189 times more light to be detected. Of course, there will be some losses due to attenuation and the angle at which the light leaves the diode, but the improvement is still expected to be two orders of magnitude better than the unpackaged case. In Chapter 4, the device will be simulated using COMSOL software, the thermal resistance can be verified, and a better approximation of the amount of light reaching the device will be determined.

CHAPTER 4:
Results

4.1 Preliminary Results with Unpackaged Device

Using the setup and results discussed in Chapter 3.1, a baseline equation that relates current and temperature to the light output could be determined. A single variable regression analysis was performed using current as the input and light intensity as the output. The results are shown in Table 4.1.

Table 4.1. Single variable regression statistics from preliminary data recorded from unpackaged device experimental runs.

Regression	Light Intensity vs. Current
Equation	Intensity = $-400.543 + 342.029 * \text{Current}(A)$
R^2	0.967368
Standard Error	195.075
Coefficient of Variation	11.2%

The p-value for current is approximately zero, but the coefficient of variation (CV) is 11.2%. This implies using the single variable equation, the results would differ on average more than 10% of the time from the actual value. This error is expected, though, since it has already been established that the temperature changes the characteristics of the model.

To determine how temperature affects the model, a multi-variable regression was performed on the data points from each experimental run. The current and temperature are the inputs, and the light intensity is the output producing Table 4.2.

Table 4.2. Multi-variable regression statistics from preliminary data recorded from unpackaged device experimental runs.

Regression	Light Intensity vs. Current and Temperature
Equation	Intensity = $-188.1 + -2.63536 * \text{Temp}(^{\circ}C) + 340.694 * \text{Current}(A)$
Adjusted R^2	0.973396
Standard Error	168.64
Coefficient of Variation	10%

The p-values for temperature and current are 0.055 and approximately 0, respectively. Based on the CV, using the current regression equation will, on average, be off approximately 10% of the time. This is still a reasonably high error and would not be useful for future current and temperature mapping in actual power systems.

This error is most likely a function of the ratio between the background noise and the light intensity measured, especially at lower currents and higher temperatures. Looking at Figure 3.4 for the 3 A case, for example, the noise is as much as 25% of the main peak. This noise-to-peak ratio increases as the temperature increases. By the 3 A 125°C run, the ratio is approximately 40%. The packaging method proposed in the previous chapter should improve this ratio and the CV.

Other potential causes of the error seen in Tables 4.1 and 4.2 could be other variables affecting the systems due to the conditions under which the experiments were performed. Environmental factors such as humidity, dust, air quality, air conditioning, and heat, to name a few, can all hurt the overall performance of the device. How to limit these additional environmental factors will not be further explored in this thesis and instead be held for future work once the actual device is built and physically tested.

4.2 Simulated Package Design Performance

After the model was built in COMSOL using the design shown in Section 3.3.5, the CAD software provided was used to simulate the thermal and electrostatic performance of the design. The results of interest from these simulations are ray tracing, electrostatics, and thermal resistance data. Based on these results, the final materials and shapes can be devised for real-world device production.

4.2.1 Optical Performance

The optical performance of the package design was the first physical aspect of the package design simulated. Optical power intensity depends on how much energy photons can deliver per unit area per time [1]. In the device design of this thesis, it is assumed the various mediums are non-absorbing, and dispersion losses are negligible. Therefore, the primary objective is to place an appropriately sized fiber optic cable at the focal point where the most light rays converge. Since it is assumed that each produced photon carries equivalent energy, increasing the available photons detected will deliver greater optical power intensity, ensuring improved light extraction performance. The light extraction performance is estimated by (4.1),

$$\eta\% = \frac{P_{det}}{P_{tot}} \times 100\% = \frac{\text{Number of Light Rays Detected}}{\text{Number of Light Rays Released}} \times 100\%, \tag{4.1}$$

where η is the efficiency, P_{det} is the amount of power detected by the fiber optic cable, and P_{tot} is the total power released by the device. Figure 4.1 shows the ray trace pattern from the device.

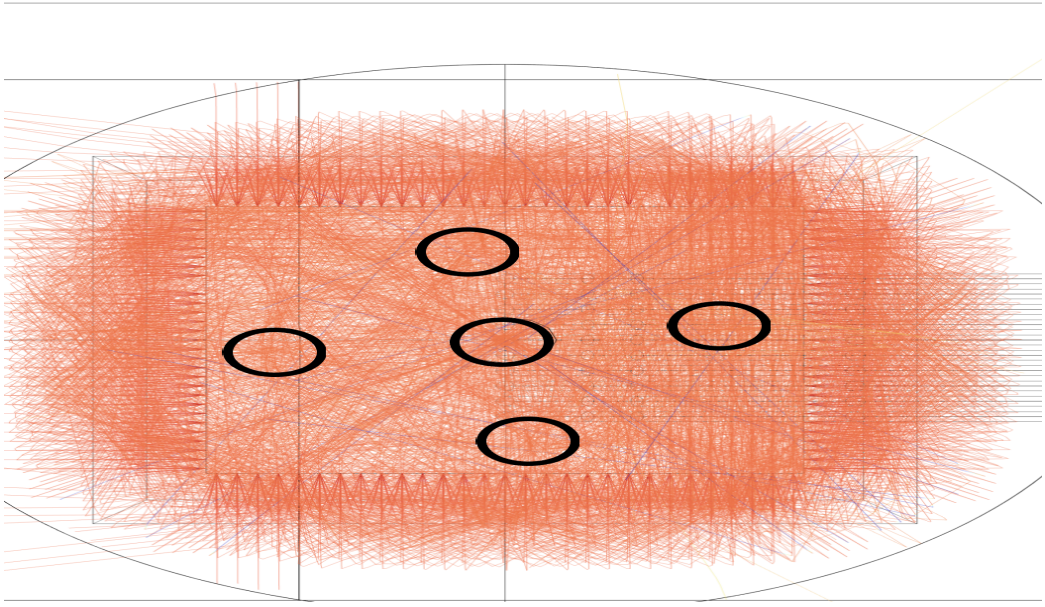

Figure 4.1. The rays primarily intersect at the five points circled. The center intersection will be investigated to determine the total rays a fiber optic cable receives.

The pattern appears to have approximately five foci in a star pattern after about 0.11 ns of run time. With the limited space, however, using a 5-to-1 fiber optic splitter cable to capture each point without special ordering a cable would be impossible. Furthermore, such a cable would be too expensive for practical use. Instead, a single fiber optic cable with a large diameter would be preferred as the middle focus point is the largest of the five foci and can be bought off the shelf at a relatively inexpensive price.

A fiber optic cable with a diameter of 1500 μm was added to the simulation at a distance of 27.7 mm to intersect the light rays at 0.11 ns shown in Figure 4.1. Using the simulated fiber optic cable, the number of light rays received by the cable could be determined. Setting the number of rays to be released from the SiC device to 3000 total light rays and using (4.1), it was determined that the device design had a detection efficiency of approximately 5.4% as 162 rays reached the simulated cable, which is about 7.5% less than the theoretical case shown in Section 3.3.5. Compared to the results shown in Section 3.2.2 for the bare SiC

die, the new device efficiency is improved by a factor of 17.4.

4.2.2 Electrostatic Performance

The electric potential physics interface was examined next. The input was 5000 V supplied to the positive terminal copper pad connected to the top of the SiC die by bonded gold wires. The simulation produced Figures 4.2 and 4.3.

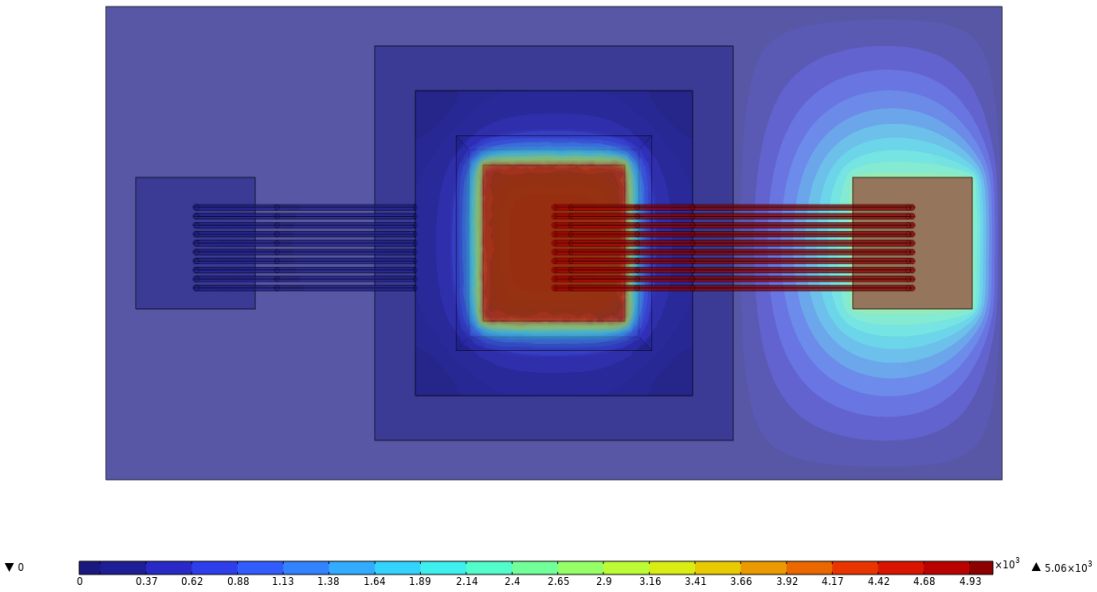

Figure 4.2. The electric potential of the modeled device shows a maximum value of 5000 V at both the positive terminal copper pad and the top of SiC die. The minimum value is 0 V, as seen at the bottom of the DBC substrate.

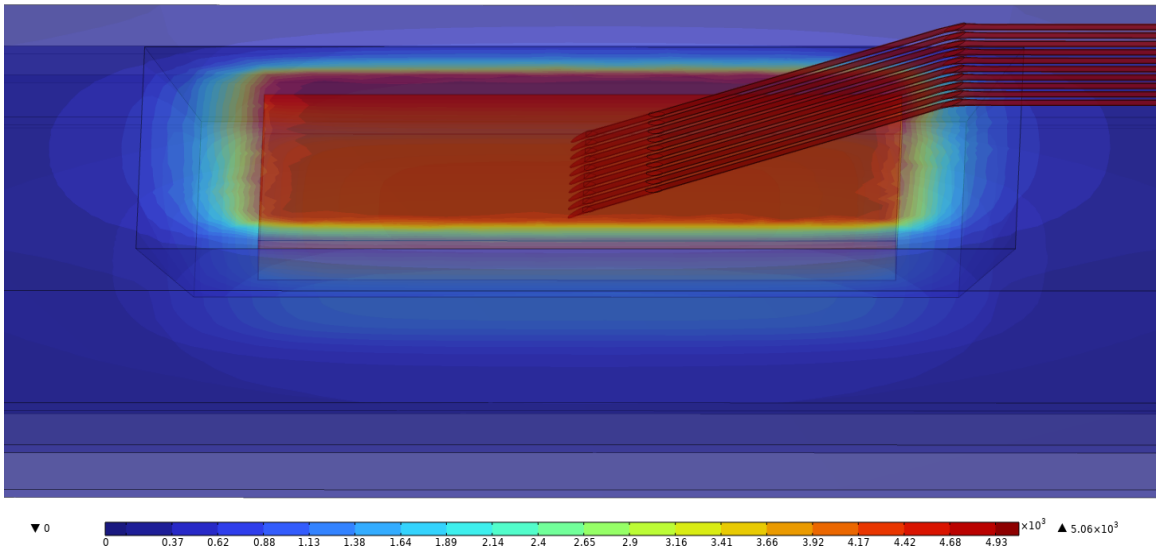

Figure 4.3. The electric potential of the device decreases throughout the cavity linearly.

Using Figure 4.3, the electric potential is at approximately 5000 V at the top of the device and drops linearly for the most part throughout the cavity radially. The electric potential reaches 0 V at the negative terminal copper pad and the copper pad the cavity is soldered to. Similarly, the electric potential decreases linearly and radially from the positive terminal copper pad.

Next, examining the electric field of the device, the electric field has a maximum electric field strength of 27 MV/m around the positive terminal copper pad. In addition, the gold bond wires and areas surrounding the positive terminal have a maximum electric field strength in the range of 1—10 MV/m, significantly higher than the dielectric strength of air at 3 MV/m [10] and can lead to electrical arcing. Figure 4.4 shows the electric field lines and strengths.

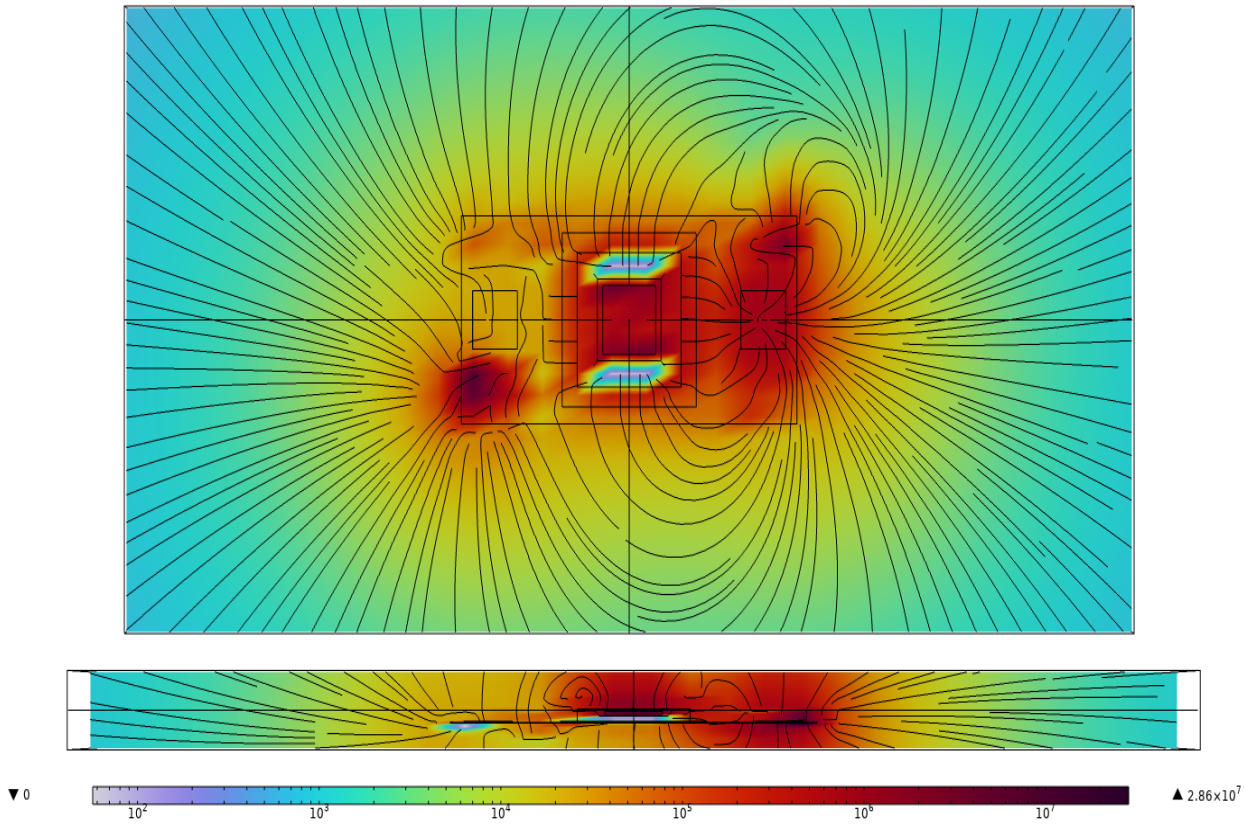

Figure 4.4. The electric field of the device with a supplied voltage of 5000 V. The maximum electric field strength is 27 MV/m concentrated on the DBC substrate, and portions above the substrate and the cavity are 1—10 MV/m. The electric field strength inside the cavity is approximately 10 kV/m.

Since the maximum electric field strength should not exceed the dielectric strength of air, the input voltage was reduced from 5000 V by 500 V increments until an input voltage of 500 V was supplied to determine a maximum for the input voltage. The resulting fields are shown in Figures A.1 through A.8 and Figure 4.5. There was no change to the shape of the electric field, and the only significant difference was the magnitude of the field across the device. Based on the results of the electrostatic simulation, it was determined that the maximum voltage input allowed is 1500 V.

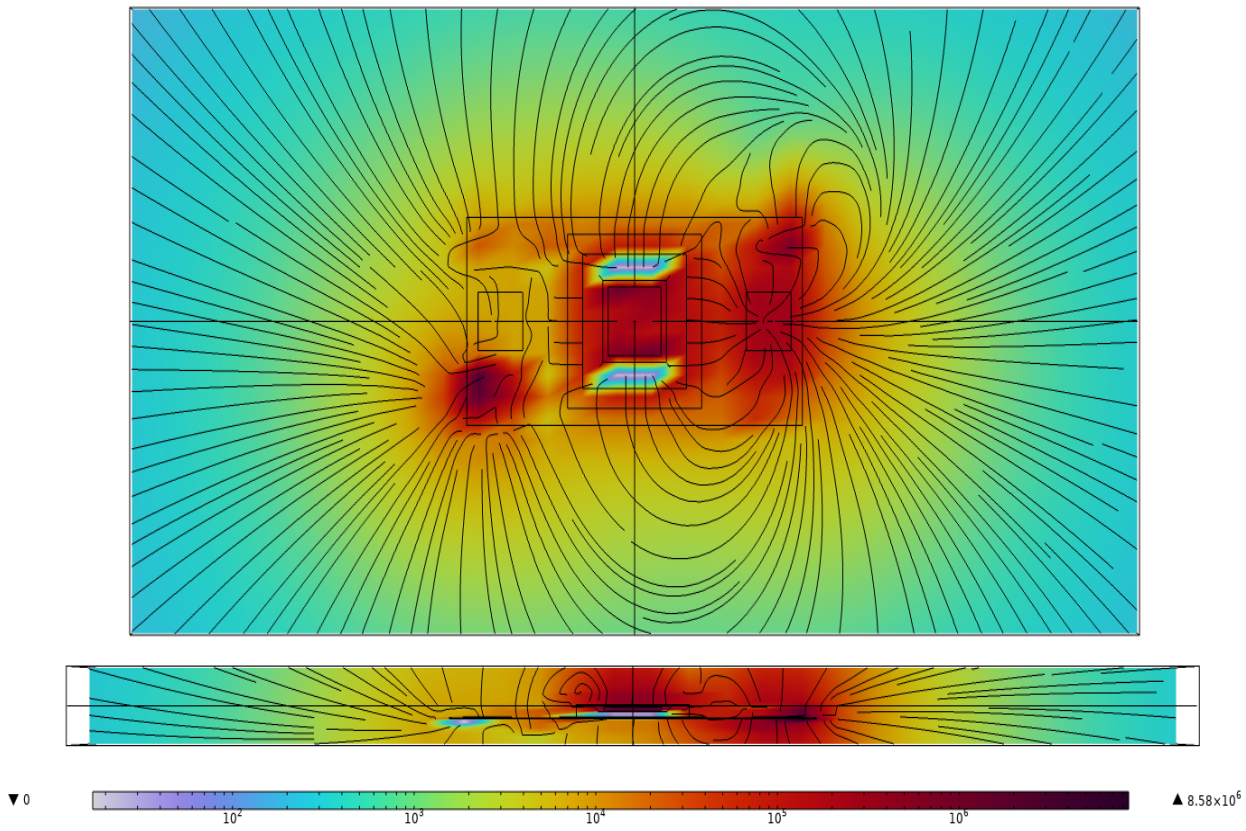

Figure 4.5. The electric field shape does not show any difference from Figure 4.4. However, outside the DBC substrate, the electric field does not exceed 1 MV/m.

From Figure 4.5, the maximum electric field strength is 8.58 MV/m inside the DBC substrate and approximately 1 MV/m outside the substrate. Since the maximum field strength outside the DBC substrate is below the dielectric strength of air, there should not be dielectric breakdown. Now that the maximum allowed input voltage is 1500 V, the electric potential of the device was once again examined. The electric potential dissipation remained the same, with only the magnitude changing from 5000 V to 1500 V, as seen in figures 4.6 and 4.7.

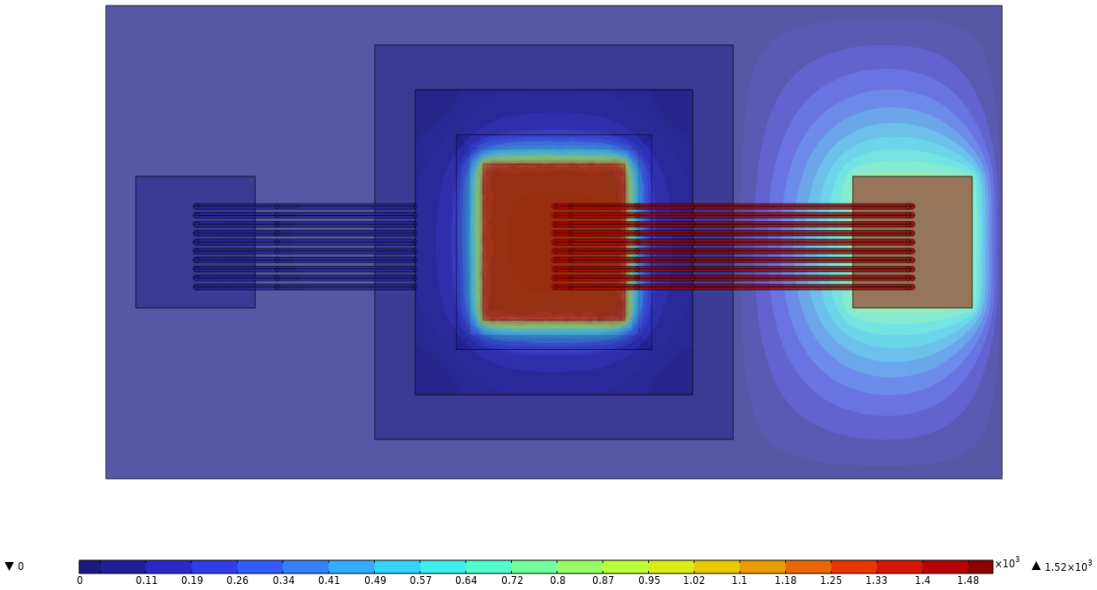

Figure 4.6. The only change is a decreased electric input to the SiC PiN diode.

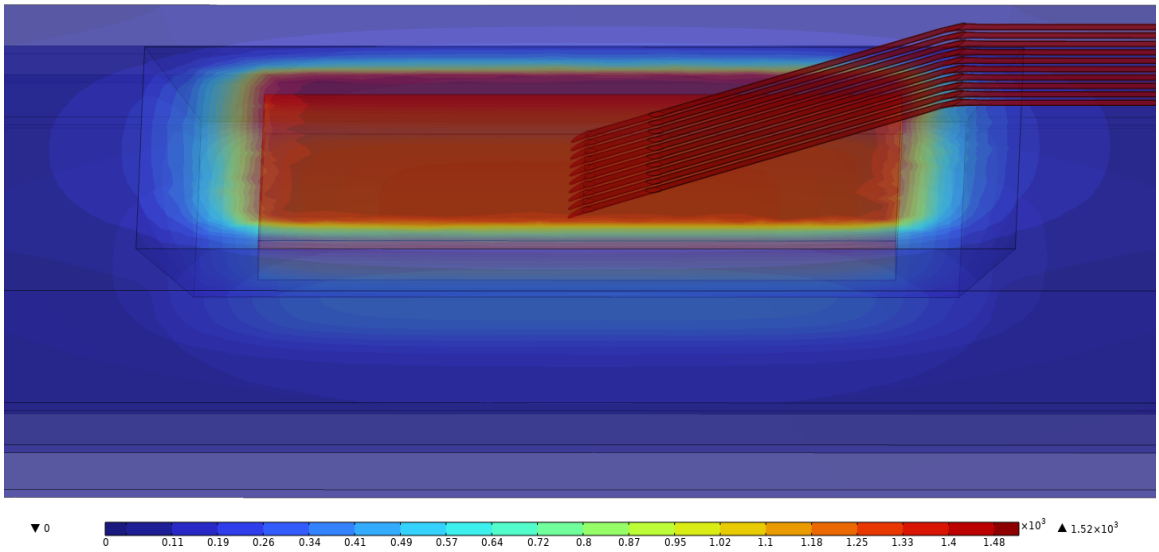

Figure 4.7. The cavity shows the same linear decrease of the electric potential as it radiates outward of the diode.

Next, the temperature distribution of the device was examined.

4.2.3 Simulated Thermal Performance

The last physics interface examined was the heat flow of the model. A heat source had to be added to the model to utilize this interface, and the bottom of the device was treated as an ideal heat sink at 293.15 K. This heat source is based on the energy losses due to the SiC diode and is computed using

$$P_{loss}/m^2 = (I_{fwd} \times V_{on} + I_{fwd}^2 \times R_{on})/m^2, \tag{4.2}$$

where V_{on} is the voltage when the diode becomes forward biased, R_{on} is the resistance of the diode, and I_{fwd} is the current when the voltage across the diode is the forward voltage found on the associated datasheet [1]. Using the data sheet provided by Naval Research

Laboratory (NRL) and Figure 3.1, V_{on} is 3.58 V, R_{on} is 0.0219 Ω, and I_{fwd} is 51.6 A when V_{fwd} is 4.64 V [16]. Using these values in (4.2) gives a P_{loss}/m^2 of 583 kW/m^2. P_{loss}/m^2 is then used as a heat source in the model and produces Figure 4.8.

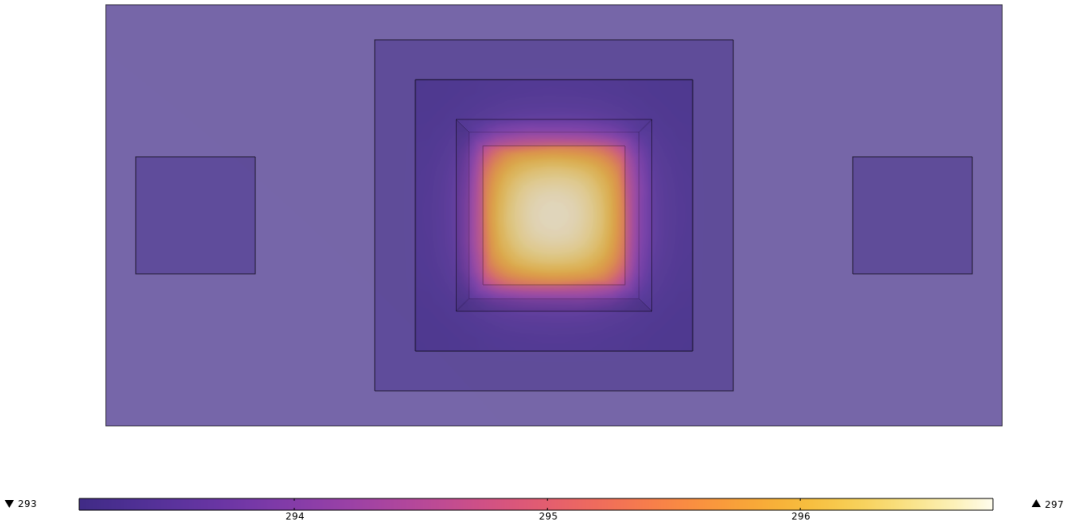

Figure 4.8. The temperature distribution of the device using an initial heat flow of 583 kW/m^2. The device has a maximum temperature of 297 K at the top of the diode and a minimum temperature of 293.15 K on the backside.

From Figure 4.8, the maximum temperature is 297 K at the top of the diode. The bottom of the device is 3.85 K less than the top of the diode with a total heat flow of 42.3 W. Using the temperature drop and the heat flow of the device, the thermal resistance of the device can be calculated using the equation

$$R_{th} = \frac{T_2 - T_1}{Q_{heat}}, \tag{4.3}$$

where $T_2 - T_1$ is the temperature difference and Q_{heat} is the heat flow [24]. Using the temperature change of 3.85 for the temperature difference and 42.3 W for the heat flow, the thermal resistance of the cavity is found to be 0.091 K/W. Using 42.3 W as the lower limit

of heat power input, 12 more tests were run at 60–300 W at 20 W increments for the heat power input, and the associated R_{th} was calculated. These are Figures A.9 through A.20 and Figure 4.9. The results are also summarized in Table 4.3

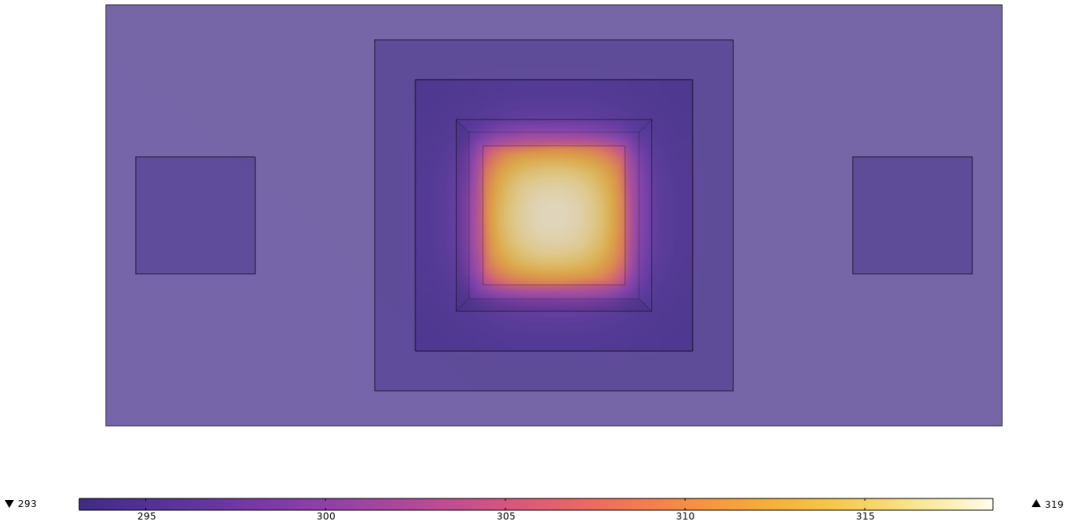

Figure 4.9. The temperature distribution of the device with a supplied heat power input of 300 W . The device has a maximum temperature of 319 K. R_{th} is 0.086 K/W.

Table 4.3. Thermal resistance calculations with multiple heat power inputs.

Heat Power Input (W)	Device Temperature (K)	Thermal Resistance (K/W)
42.3	297	0.091
60	298	0.081
80	300	0.086
100	301	0.079
120	303	0.082
140	305	0.085
160	307	0.087
180	308	0.083
200	310	0.084
220	312	0.086
240	313	0.083
260	315	0.084
280	317	0.085
300	319	0.086

Based on the R_{th} values from Table 4.3, the device design will have sufficient ability for heat extraction, enabling higher power operations. This will be particularly useful because the epoxy has a maximum operating temperature of $150°C$. Extended periods of operation above this temperature could result in discoloration and breakdown of the epoxy rendering the device useless for light extraction. With low thermal resistance, a decent heat sink should keep the device within the allowable temperature.

THIS PAGE INTENTIONALLY LEFT BLANK

CHAPTER 5:
Conclusion and Future Work

5.1 Conclusion

The research presented in this thesis primarily investigated how to improve light production of a SiC PiN diode in high-power system operations. A preliminary investigation was conducted on a bare SiC diode at various temperatures and currents. A linear regression analysis was utilized from this initial data to map the light intensity a fiber optic cable received to the applied current and temperature. With the baseline study conducted, the method and material needed for encapsulation of the diode were decided upon based on several factors, such as handling high heat and voltage, keeping the cost reasonable, and improving light production. The material, the properties of the material, and the geometries of the device were then modeled using COMSOL to test the capability and improvement of the device and to determine future considerations for the device. Once modeled, the CAD software was used to simulate the device. The simulations showed the light received by the fiber optic cable could be improved from 0.31% of the total light produced to 5.4%, the maximum input voltage is 1500 V due to electric field strengths, and the thermal resistance of the device is around 0.083 K/W.

5.2 Future Work

With all the research before the build is completed, the next step is to build the fully encapsulated device. This will require aluminum (Al) sheet fabrication to develop the wells for the SiC diode, encapsulation epoxy resin, a plano-convex lens, large caliber fiber optic cables, gold bond wires, copper pads for both the Al wells and positive/negative terminals, a DBC substrate, and a heat sink to keep the material from reaching over $150°C$. Once appropriately configured, a new test needs to be conducted using the same steps from Chapter 3 with the results compared to the baseline. The further regression analysis can act as the new baseline with a theoretically less CV. Next, the device will need to be connected to a power system. Once connected to a power system, a control system with a feedback loop will need to be determined that will control the voltage output of the power system.

THIS PAGE INTENTIONALLY LEFT BLANK

APPENDIX: Additional Figures

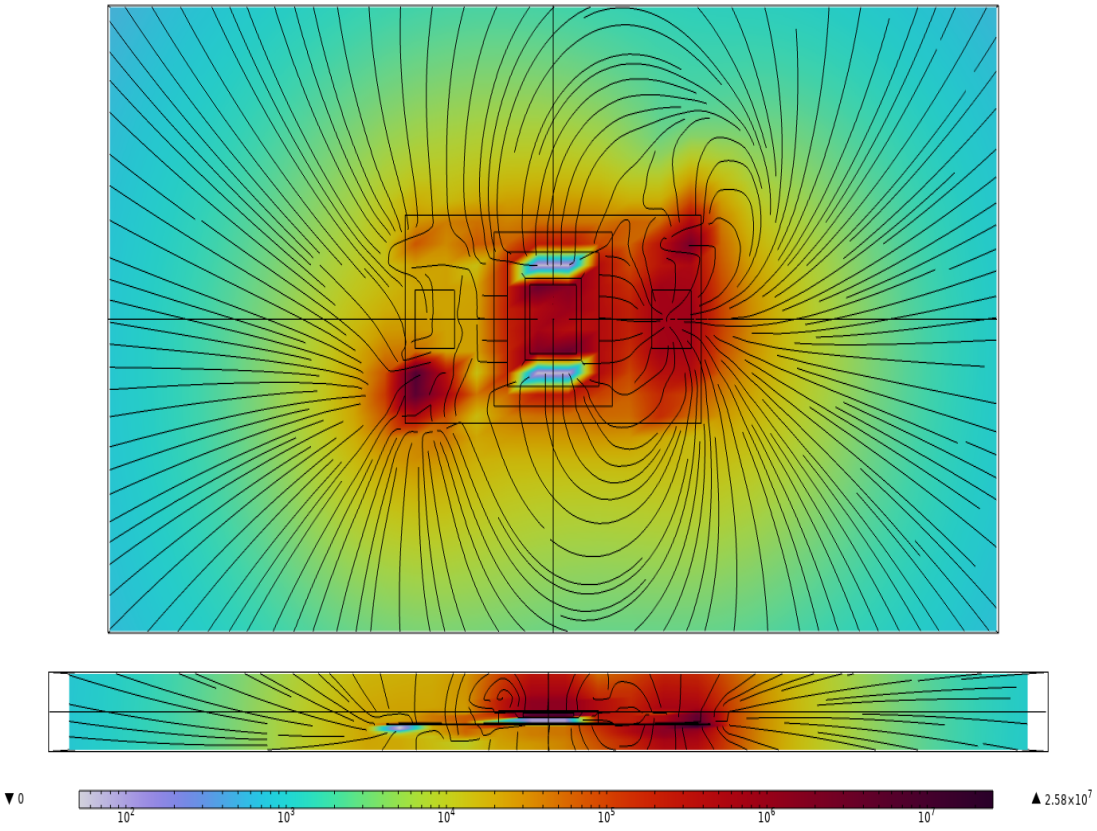

Figure A.1. The electric field of the device with a supplied voltage of 4500 V. The maximum electric field strength is 25.8 MV/m concentrated on the DBC substrate. Areas outside the substrate and above the cavity are still in the 1—10 MV/m range.

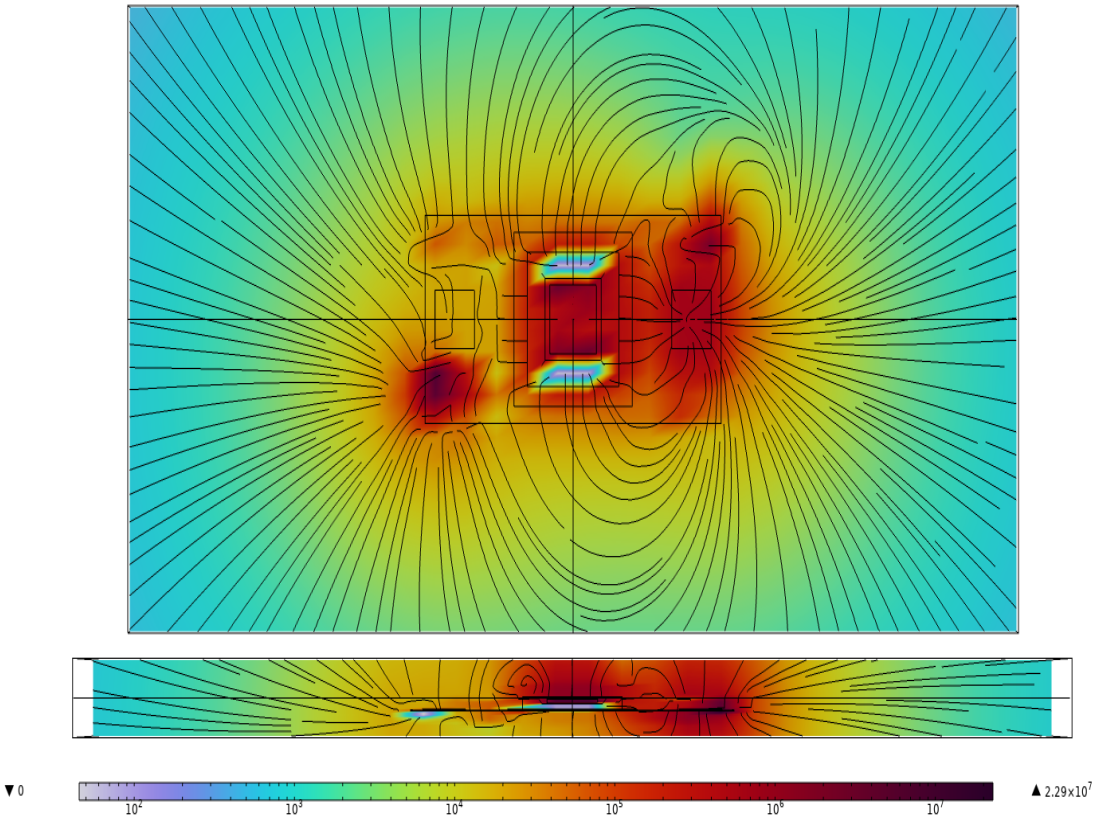

Figure A.2. The electric field of the device with a supplied voltage of 4000 V. The maximum electric field strength is 22.9 MV/m still inside the DBC substrate. Areas outside the substrate and above the cavity are in the 1—8 MV/m range.

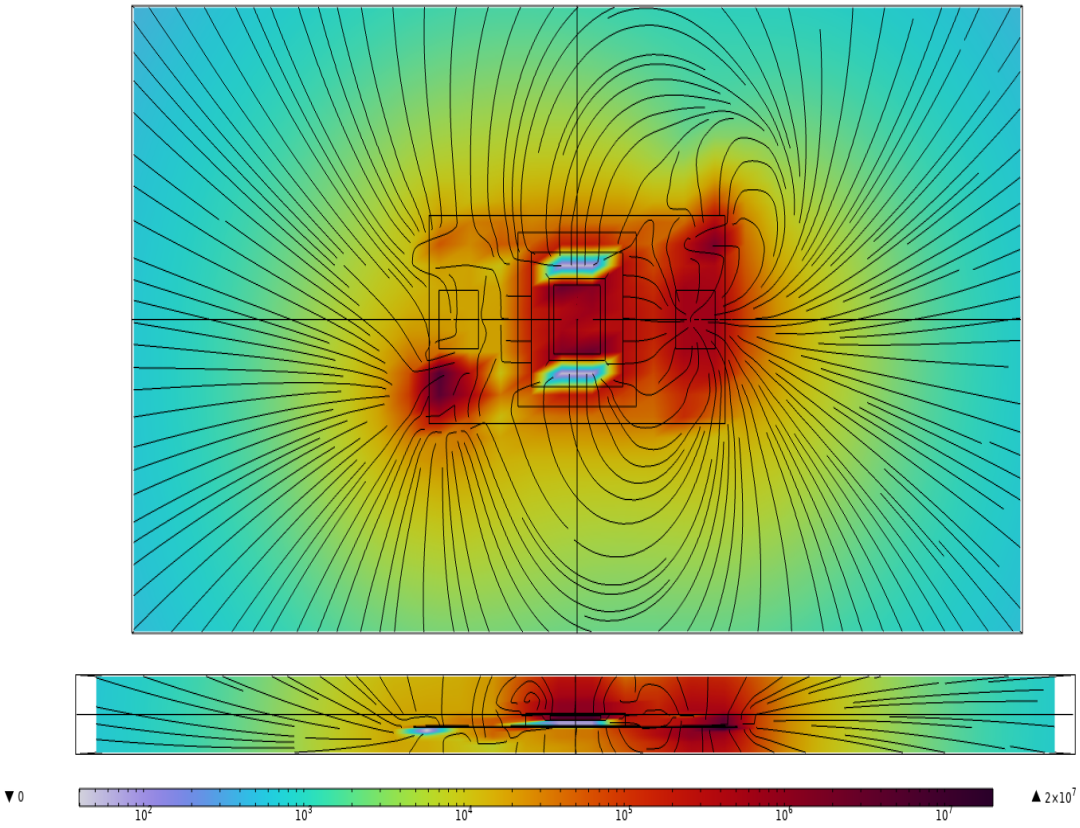

Figure A.3. The electric field of the device with a supplied voltage of 3500 V. The maximum electric field strength is 20 MV/m concentrated on the DBC substrate. Areas outside the substrate and above the cavity are in the 1—5 MV/m range.

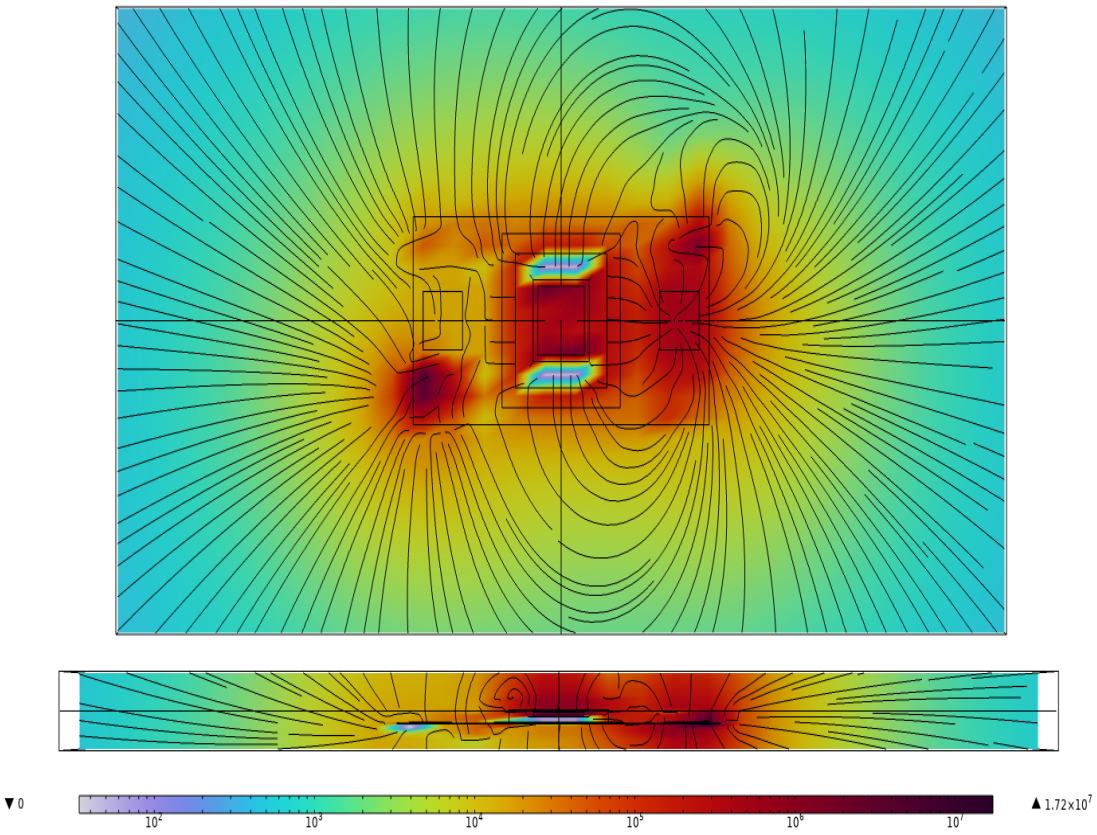

Figure A.4. The electric field of the device with a supplied voltage of 3000 V. The maximum electric field strength is 17.2 MV/m concentrated on the DBC substrate. Areas outside the substrate and above the cavity are in the 1—3 MV/m range.

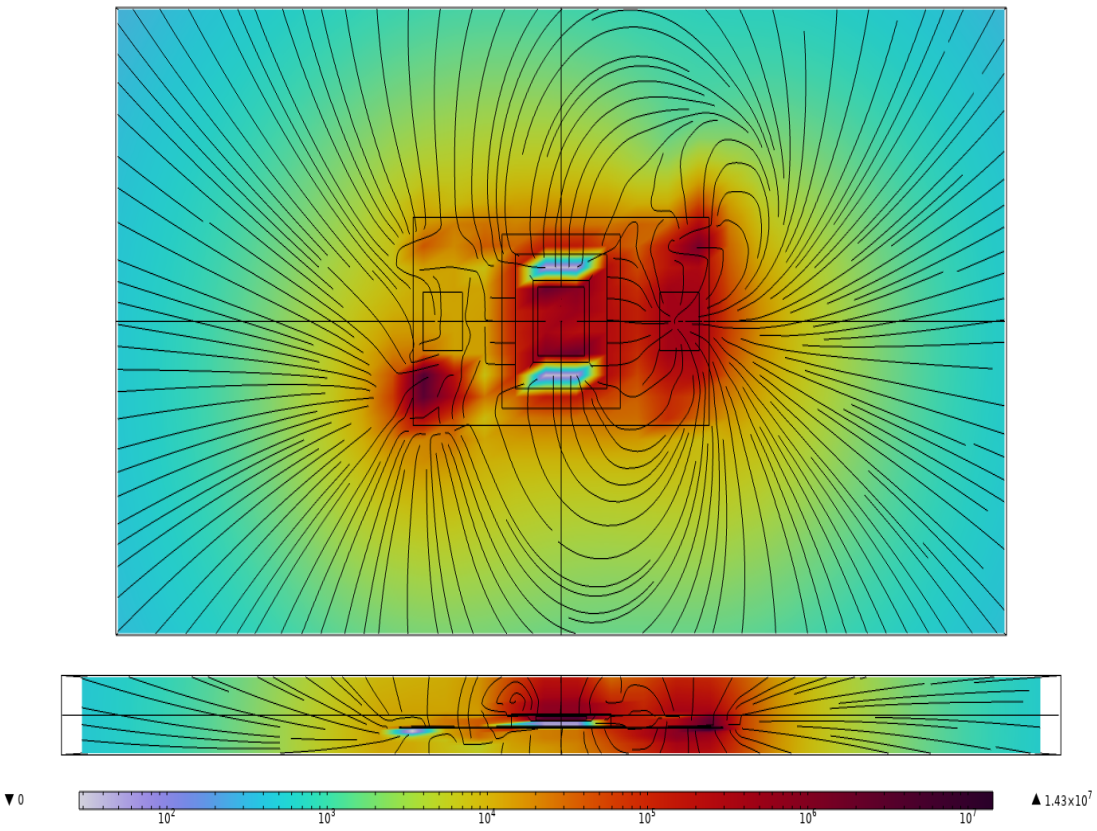

Figure A.5. The electric field of the device with a supplied voltage of 2500 V. The maximum electric field strength is 14.3 MV/m concentrated on the DBC substrate. Areas outside the substrate and above the cavity are still in the 1—3 MV/m range.

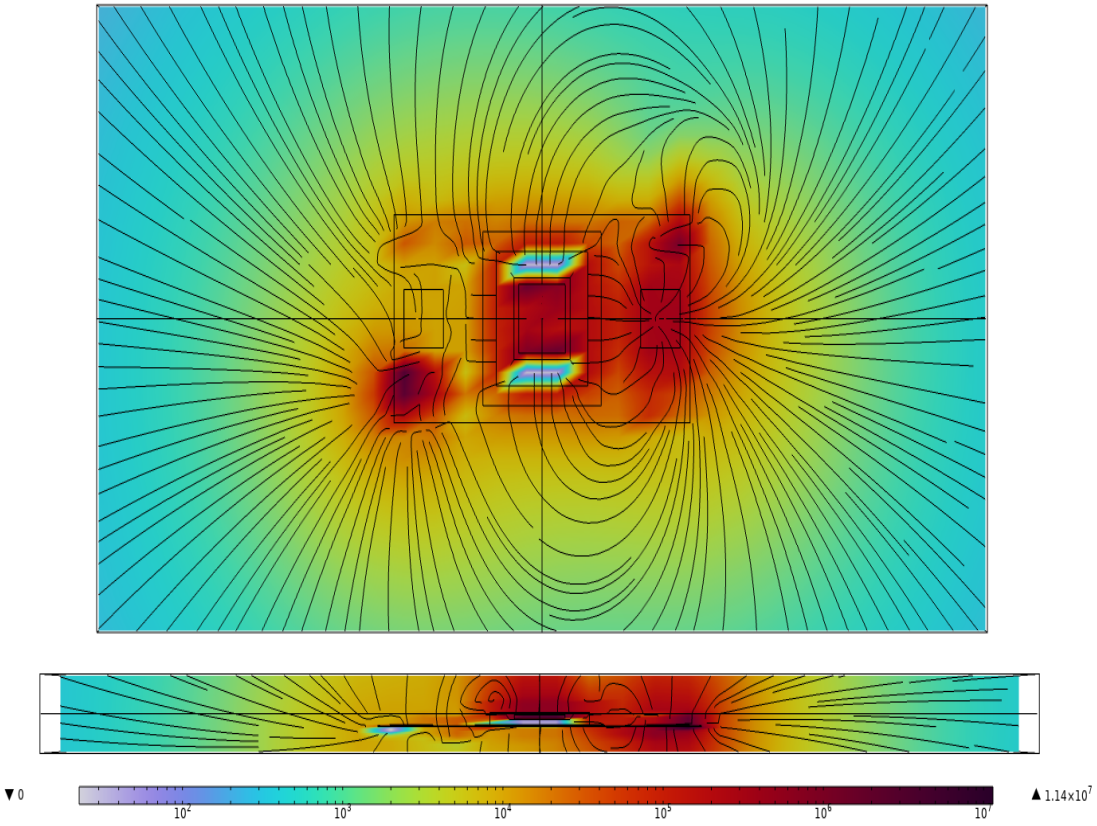

Figure A.6. The electric field of the device with a supplied voltage of 2000 V. The maximum electric field strength is 11.4 MV/m concentrated on the DBC substrate. Areas outside the substrate and above the cavity are in the 1—2 MV/m range.

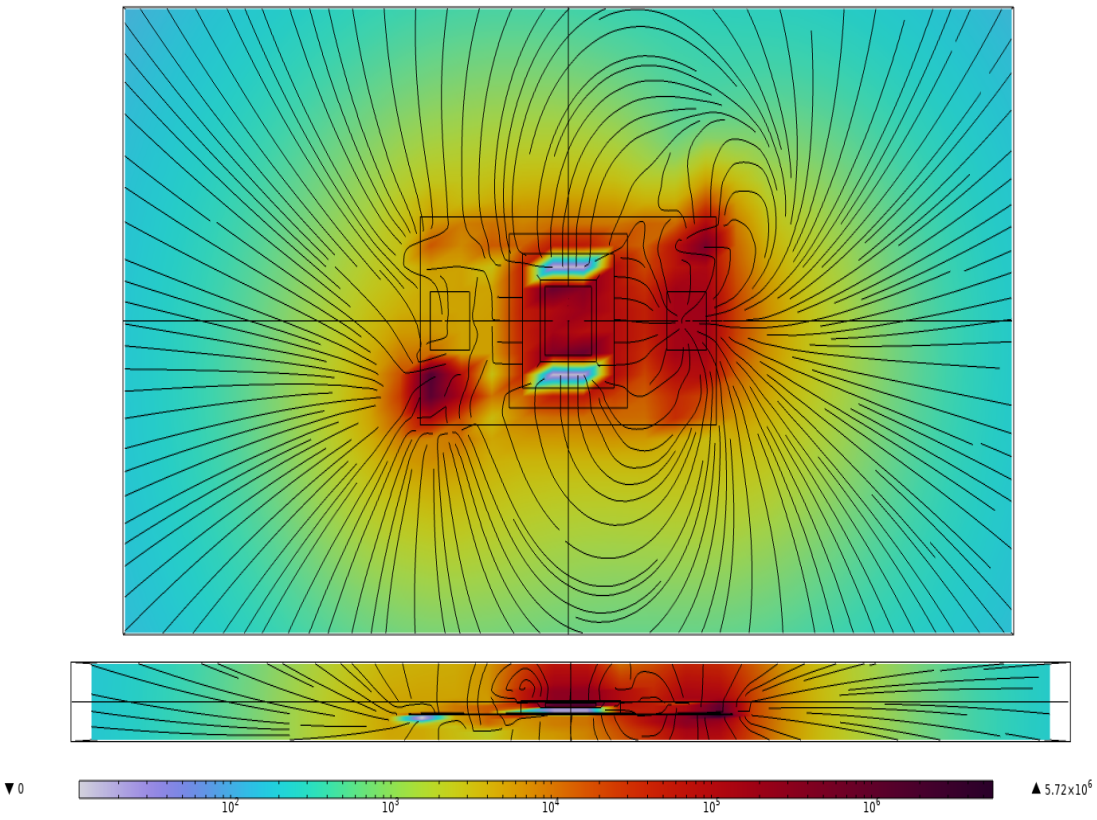

Figure A.7. The electric field of the device with a supplied voltage of 1000 V. The maximum electric field strength is 5.72 MV/m concentrated on the DBC substrate. The maximum field outside the substrate does not exceed 1 MV/m.

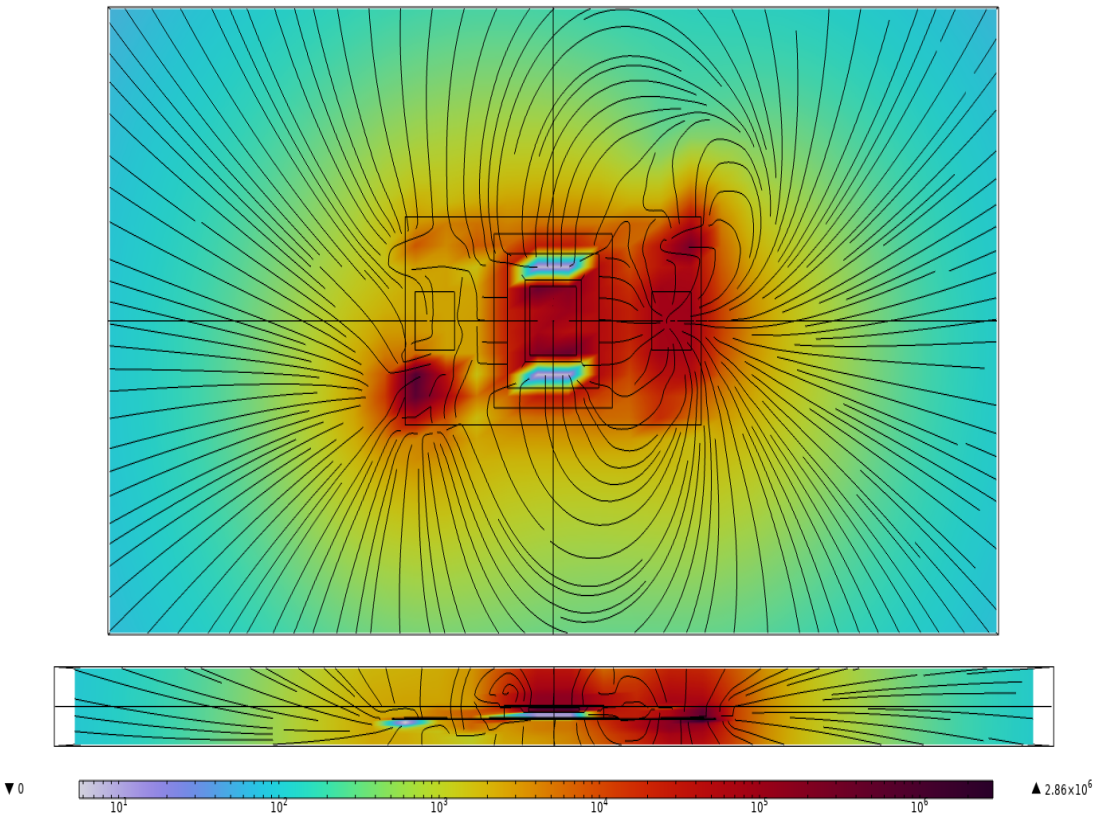

Figure A.8. The electric field of the device with a supplied voltage of 500 V. The maximum electric field strength is 2.86 MV/m concentrated on the DBC substrate. The maximum field outside the substrate does not exceed 1 MV/m.

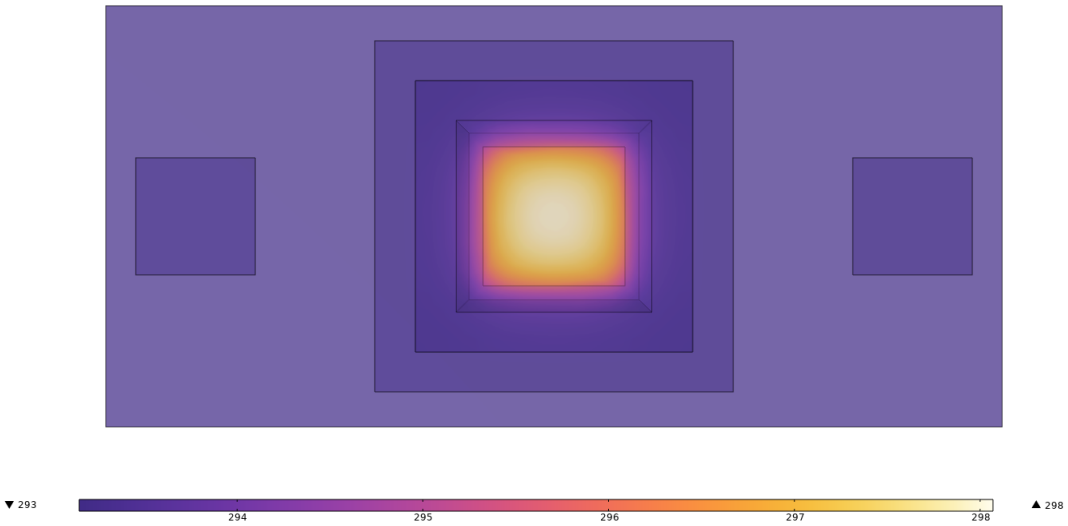

Figure A.9. The temperature distribution of the device with a supplied heat power input of 60 W . The device has a maximum temperature of 298 K. R_{th} is 0.081 K/W.

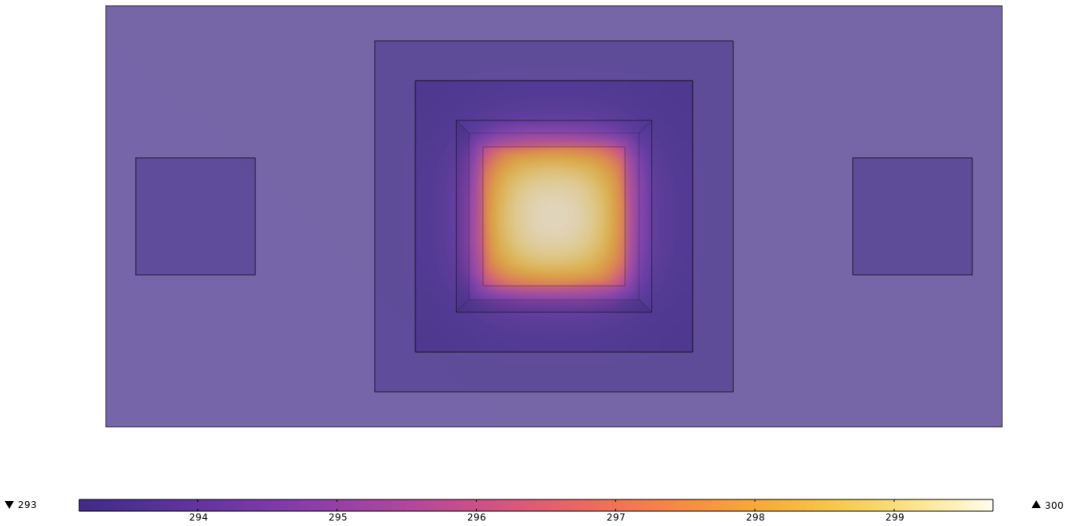

Figure A.10. The temperature distribution of the device with a supplied heat power input of 80 W . The device has a maximum temperature of 300 K. R_{th} is 0.086 K/W.

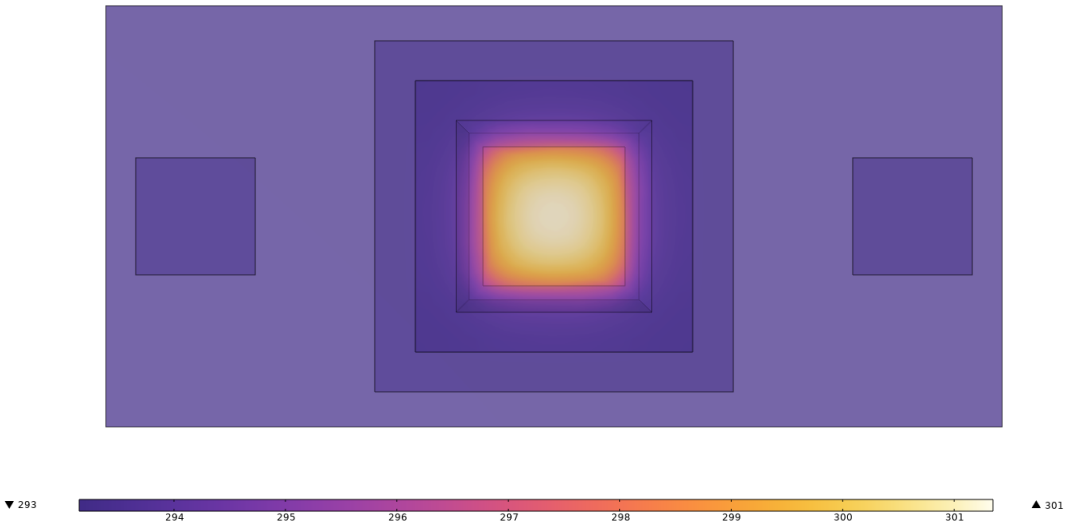

Figure A.11. The temperature distribution of the device with a supplied heat power input of 100 W . The device has a maximum temperature of 301 K. R_{th} is 0.079 K/W.

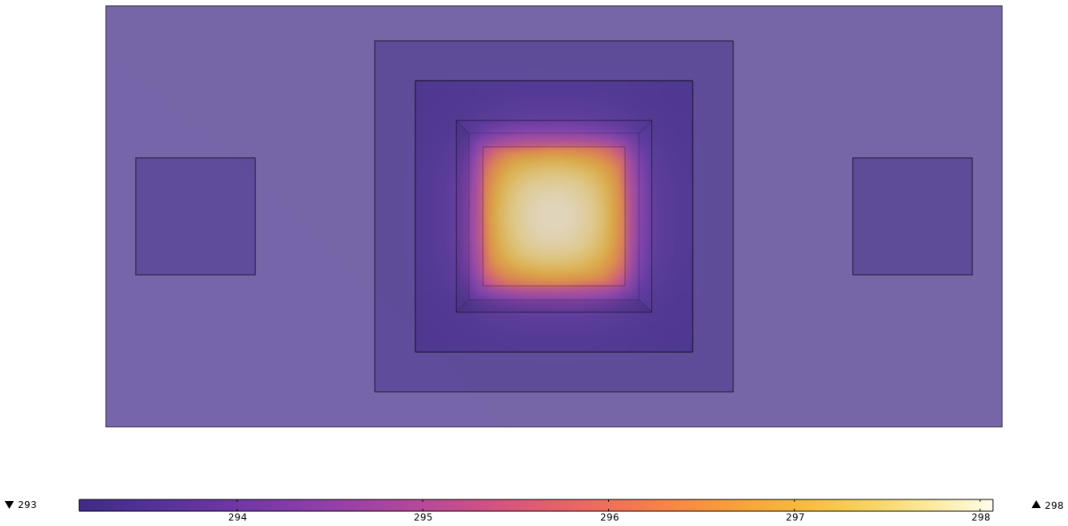

Figure A.12. The temperature distribution of the device with a supplied heat power input of 120 W . The device has a maximum temperature of 303 K. R_{th} is 0.082 K/W.

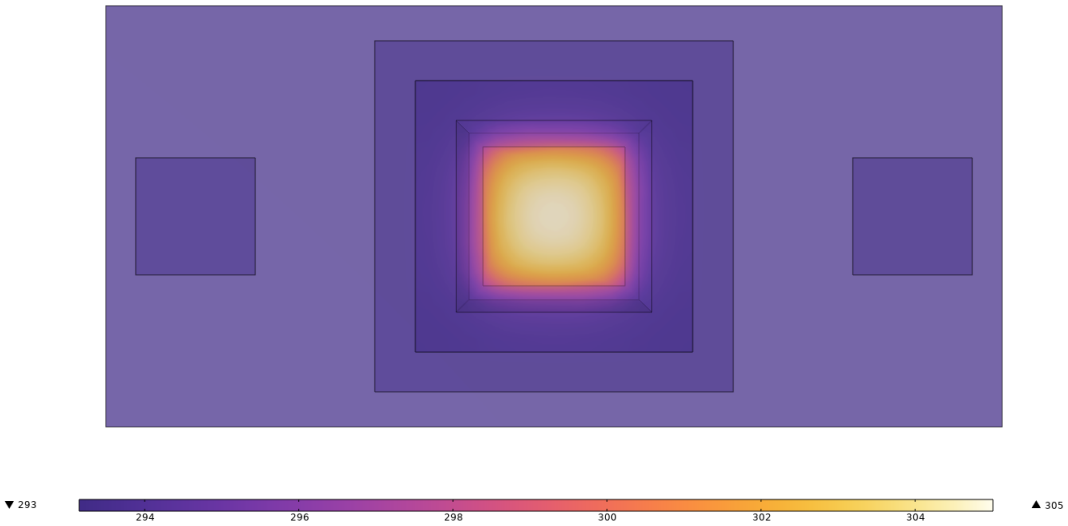

Figure A.13. The temperature distribution of the device with a supplied heat power input of 140 W . The device has a maximum temperature of 305 K. R_{th} is 0.085 K/W.

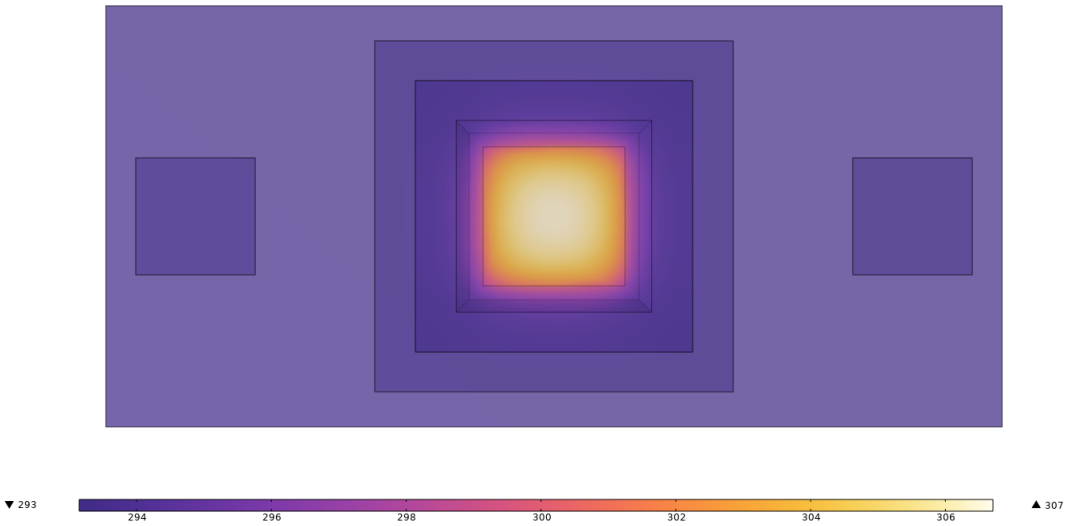

Figure A.14. The temperature distribution of the device with a supplied heat power input of 160 W . The device has a maximum temperature of 307 K. R_{th} is 0.087 K/W.

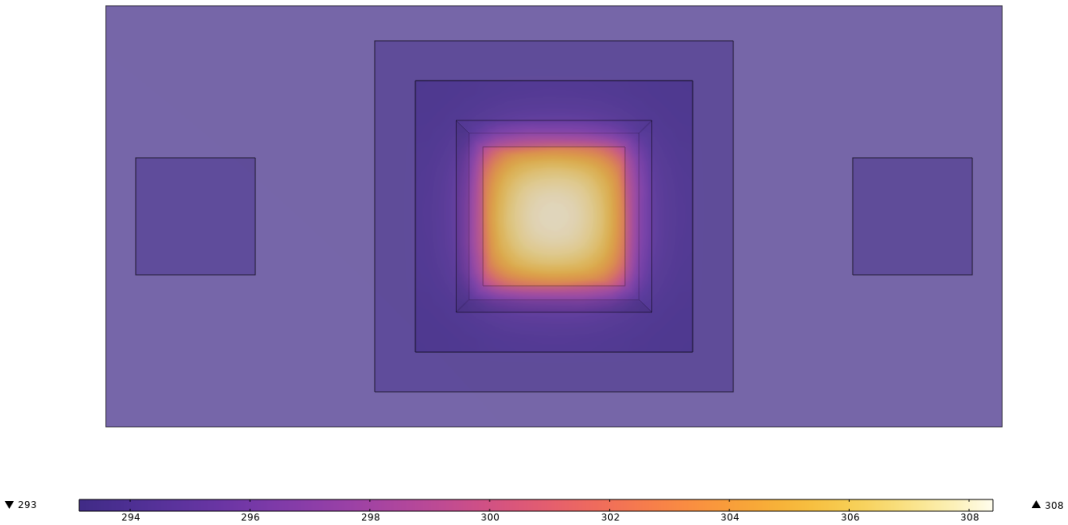

Figure A.15. The temperature distribution of the device with a supplied heat power input of 180 W . The device has a maximum temperature of 308 K. R_{th} is 0.083 K/W.

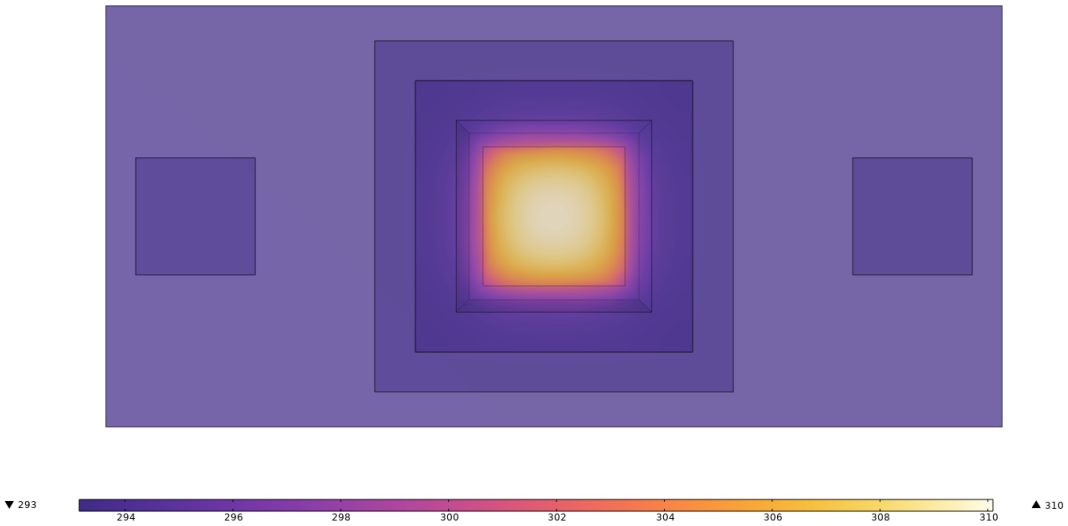

Figure A.16. The temperature distribution of the device with a supplied heat power input of 200 W . The device has a maximum temperature of 310 K. R_{th} is 0.084 K/W.

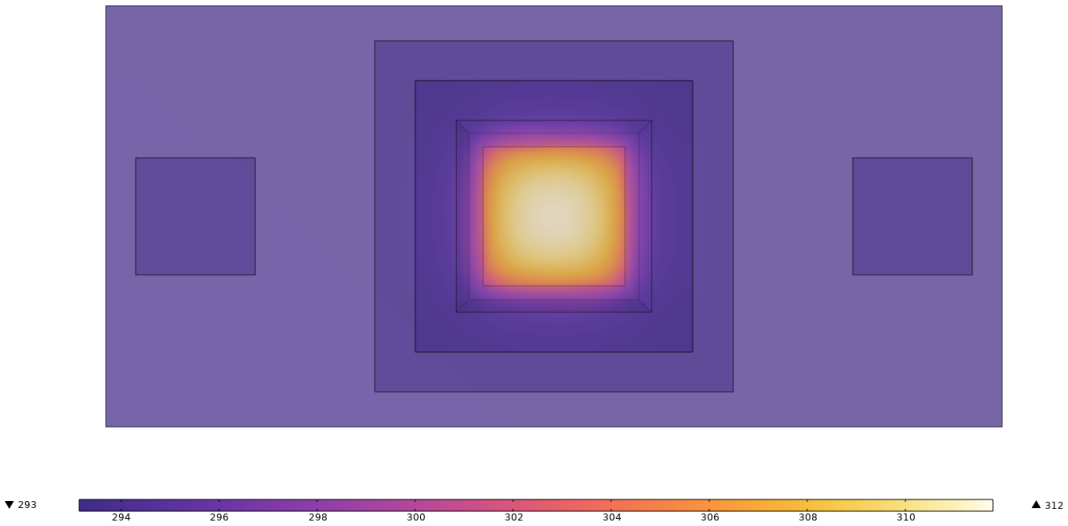

Figure A.17. The temperature distribution of the device with a supplied heat power input of 220 W . The device has a maximum temperature of 312 K. R_{th} is 0.086 K/W.

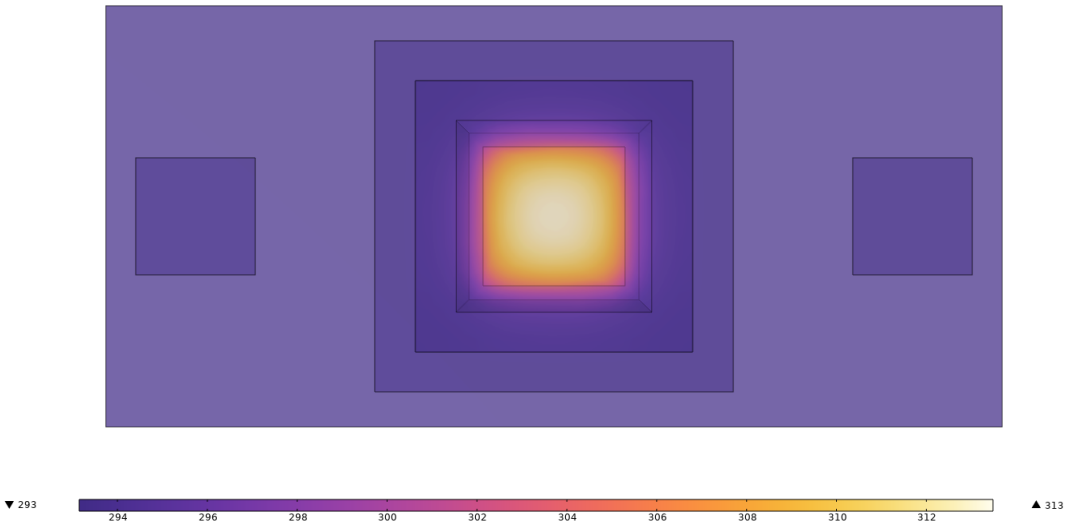

Figure A.18. The temperature distribution of the device with a supplied heat power input of 240 W . The device has a maximum temperature of 313 K. R_{th} is 0.083 K/W.

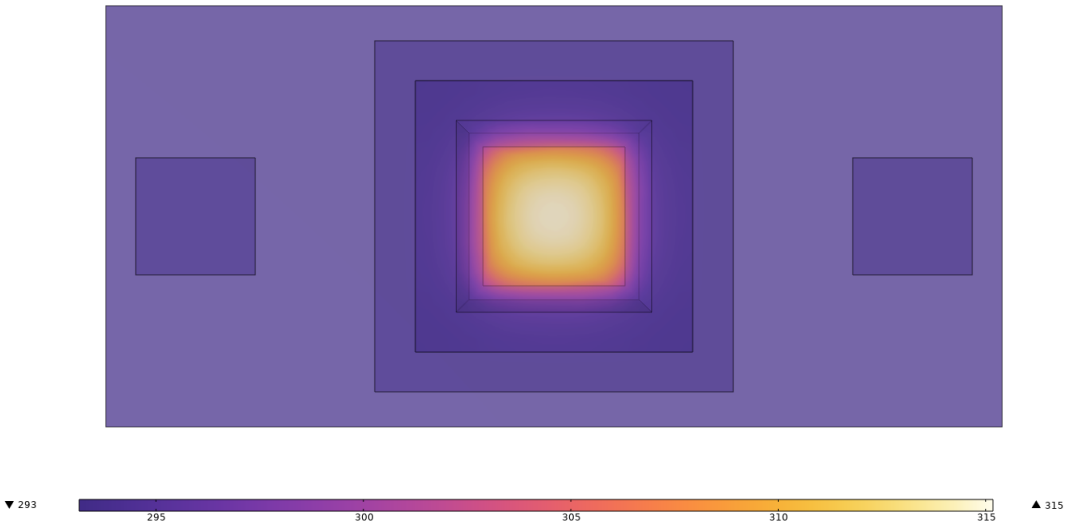

Figure A.19. The temperature distribution of the device with a supplied heat power input of 260 W . The device has a maximum temperature of 315 K. R_{th} is 0.084 K/W.

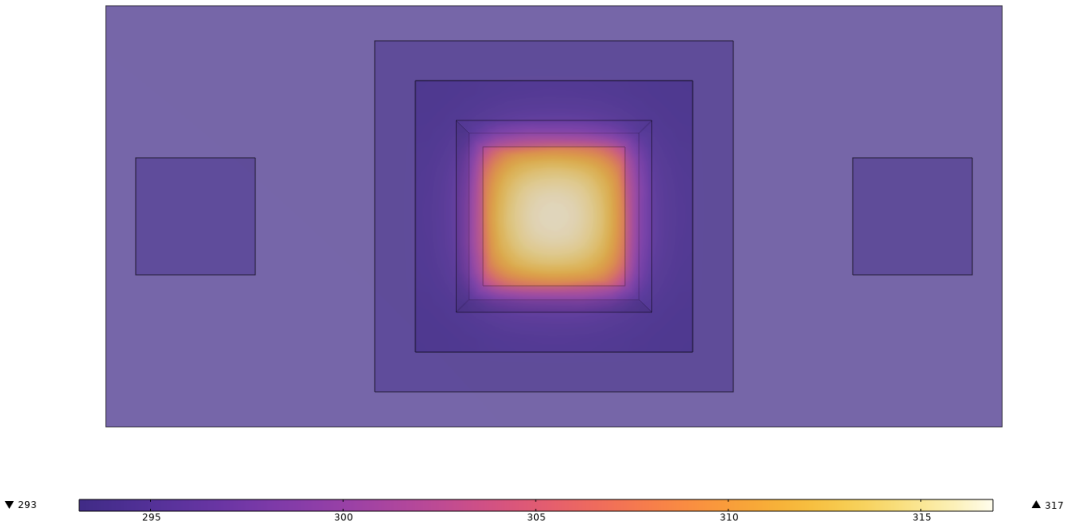

Figure A.20. The temperature distribution of the device with a supplied heat power input of 280 W . The device has a maximum temperature of 317 K. R_{th} is 0.085 K/W.

List of References

[1] B. J. Baliga, *Fundamentals of Power Semiconductor Devices*, 1st ed. New York, NY, USA: Springer, 2008.

[2] J. Winkler, J. Homoth, and I. Kallfass, "Electroluminescence in power electronic applications: Utilization of p-n junctions in power semiconductors as unintentional light emitting diodes for current and temperature sensing," *Proc. 31st Int. Electric Veh. Symp. Int. Electric Veh.*, Oct 2018.

[3] M. Broeg, "Current and temperature sensing via light emission from gan pn junctions," M.S. thesis, Dept. of Elec. and Comp. Eng., NPS, Monterey, CA, USA, 2019 [Online]. Available: https://hdl.handle.net/10945/71601

[4] J. L. Williams, "Gan light emission for control system feedback," M.S. thesis, Dept. of Elec. and Comp. Eng., NPS, Monterey, CA, USA, 2020 [Online]. Available: https://hdl.handle.net/10945/70788

[5] J. Johnston, "Gan light emission controlled dc-dc converter," M.S. thesis, Dept. of Elec. and Comp. Eng., NPS, Monterey, CA, USA, 2022 [Online]. Available: https://hdl.handle.net/10945/71485

[6] C. Robinson, "Electrooptical characteristics of sic mosfet body diode and gan power diode," M.S. thesis, Dept. of Elec. and Comp. Eng., NPS, Monterey, CA, USA, 2022.

[7] M. Östling, R. Ghandi, and C. Zetterling, "SiC power devices — Present status, applications and future perspective," in *2011 IEEE 23rd International Symposium on Power Semiconductor Devices and ICs*, 2011 [Online]. Available: https://ieeexplore-ieee-org.libproxy.nps.edu/abstract/document/5890778

[8] U. K. Mishra and J. Singh, *Semicondcutor Device Physics and Design*, 1st ed. New York, NY, USA: Springer, 2008.

[9] F. Rana, "Semiconductor Light Emitting Diodes and Solid State Lighting," Accessed February 5, 2023 [Online]. Available: https://courses.cit.cornell.edu/ece533/Lectures/handout7.pdf

[10] P. Tipler and G. Mosca, *Physics for Scientists and Engineers*, 6th ed. New York, NY, USA: W. H. Freeman and Company, 2008.

[11] RP Photonics Encycopedia, "Sellmeier Formula," Accessed Nov. 20, 2022 [Online]. Available: https://www.rp-photonics.com/sellmeier_formula.html

[12] M. N. Polyanskiy. Refractive index database. [Online]. Available: https://refractiveindex.info

[13] Brown University, “Fresnel’s Equations for Reflection and Transmission,” Accessed February 20, 2022 [Online]. Available: https://www.brown.edu/research/labs/mittleman/sites/brown.edu.research.labs.mittleman/files/uploads/lecture13_0.pdf

[14] Newport Corporation, “Plano-Convex Lenses,” Accessed Nov. 20, 2022 [Online]. Available: https://www.newport.com/c/plano-convex-lenses

[15] C. Chen, F. Luo, and Y. Kang, “A review of sic power module packaging: Layout, material system and integration,” *CPSS Transactions on Power Electronics and Applications*, vol. 2, no. 3, Sep 2017 [Online]. doi.https://doi.org/10.24295/CPSSTPEA.2017.00017.

[16] Cree, Inc., N00014-02-C-0302 CLIN 0002, Items 9,10, &11 PiN Diode Deliverables, 2021.

[17] J. Caldwell, A. Giles, D. L. D. Carrier, K. Moumanis, B. A. Hull, R. Stahlbush, R. L. Myers-Ward, J. J. Dubowski, and M. Verhaegen, “Experimental evidence for mobile luminescence center mobility on partial dislocations in 4h-sic using hyperspectral electroluminescence imaging,” *Applied Physics Letters*, vol. 102, June 2013 [Online]. doi: https://doi.org/10.1063/1.4810909.

[18] M. Polyanskiy, “Optical constants of silicon carbide (sic),” Accessed February 12, 2022 [Online]. Available: https://refractiveindex.info/?shelf=main&book=SiC&page=Wang-4H-e

[19] M. Polyanskiy, “Optical constants of silicon carbide (sic),” Accessed February 12, 2022 [Online]. Available: https://refractiveindex.info/?shelf=main&book=SiC&page=Wang-4H-o

[20] Epoxies, ETC, 20-3401 Medical, Optical and Semiconductor Grade Epoxy Resin [Online]. Available: https://epoxies.com/wp-content/uploads/2022/05/20-3401.pdf

[21] M. Porter, private communication, Oct. 2022.

[22] Thorlabs, "LA1540-A - N-BK7 Plano-Convex Lens, 01/2, f = 15 mm, AR Coating: 350 - 700 nm". Available: https://www.thorlabs.com/drawings/742c24841518c18f-B2D86EC2-A6D0-3577-9CF80D6382030841/LA1540-A-AutoCADPDF.pdf

[23] M. Polyanskiy, “Optical constants of bk7,” Accessed March 15, 2022 [Online]. Available: https://refractiveindex.info/?shelf=glass&book=BK7&page=SCHOTT

[24] Omni Calculator, “What is thermal resistance,” Accessed on Jan. 11 2023 [Online]. Available: https://www.omnicalculator.com/physics/thermal-resistance

Initial Distribution List

1. Defense Technical Information Center
   Ft. Belvoir, Virginia

2. Dudley Knox Library
   Naval Postgraduate School
   Monterey, California